Nonlinear finite element and analytical modelling of reinforced concrete filled steel tube columns under axial compression loading

Haytham F. Isleem [a],[**], Naga Dheeraj Kumar Reddy Chukka [b], Alireza Bahrami [c],[*], Solomon Oyebisi [d], Rakesh Kumar [e], Tang Qiong [a]

[a] School of Applied Technologies, Qujing Normal University, Qujing, 655011, Yunnan, China
[b] Department of Civil Engineering, Aditya College of Engineering and Technology, Surampalem, India
[c] Department of Building Engineering, Energy Systems and Sustainability Science, Faculty of Engineering and Sustainable Development, University of Gävle, 801 76 Gävle, Sweden
[d] Department of Civil Engineering, Covenant University, PMB 1023, Ota, Nigeria
[e] Department of Civil Engineering, National Institute of Technology Patna, India

ARTICLE INFO

ABSTRACT

Local buckling of steel and excessive spalling of concrete have necessitated the need for the evaluation of reinforced concrete columns subjected to axial compression loading. Thus, this study investigates the behaviour of concrete filled steel tube (CFST) columns and reinforced concrete filled steel tube (RCFST) columns under the axial compression using the finite element modelling and machine learning (ML) techniques. To achieve this aim, a total of 85 columns from existing studies were analysed utilising the finite element modelling. The ultimate load of the generated datasets was predicted employing various ML techniques. The findings showed that the columns' compressive strength, ductility, and toughness were improved by reducing transverse reinforcement spacing, increasing the number of reinforcing bars, and increasing the thickness and yield strength of outer steel tube. Under the axial compression loading, the finite element modelling analysis provided an accurate assessment of the structural performance of the RCFST columns. Compared to other ML approaches, gradient boosting exhibited the best performance metrics with R^2 and root mean square error values of 99.925% and 0.00708 and 99.863% and 0.00717 respectively in training and testing stages, to predict the columns' ultimate load. Overall, gradient boosting can be applied in the ultimate load prediction of CFST and RCFST columns under the axial compression, conserving resources, time, and cost in the investigation of the ultimate load of columns through laboratory testing.

1. Introduction

Numerous civil engineering structures are assessed as closed systems where additional mass spatial distribution can vary according to the basic continuity and energy equations [1]. Environmental forces like wind and earthquakes can affect civil engineering structures, which can change their modal features including natural frequency and mode shape [2]. These have led to the principles of concrete-filled and reinforced concrete filled steel-tube columns to stop the concrete from buckling or collapsing during an earthquake and seismicity. The benefits of reinforced concrete filled steel tube (RCFST) columns in the building industry have drawn increased attention from academics and researchers. The behaviour and strength of RCFST columns under axial compression were investigated [3]. The results demonstrated that for axially compressed circular RCFST columns, the steel tube yielded at the peak load point, whereas for square RCFST columns, the steel tube yielded at the post peak stage. Besides, the ductility decreased with increasing the compressive strength for both circular and square RCFST columns [3]. In another study, CFST columns displayed substantial seismic resistance behaviour and offered significant energy dissipation under earthquake stress [4]. A relevant study examined how to improve the compressive behaviour of reinforced concrete (RC) walls under both

---

centric and eccentric loads [5]. The findings revealed that, in comparison to control specimens, the expanded or glass fibre wire mesh ferrocement tested specimens increased ultimate loads. Compared to glass fibre mesh reinforcement, expanded steel wire reinforcement had a higher ductility ratio. However, in comparison to expanded wire mesh, glass fibre wire mesh exhibited higher initial breaking loads, serviceability loads, load carrying capacities, and energy absorption. Finally, the structural performance of nonlinear ferrocement RC walls was accurately estimated by the finite element modelling [5]. El-Sayed [6] studied the axial compression behaviour of ferrocement geopolymer HSC columns. The ferrocement geopolymer HSC columns performed as expected, according to the results. Additionally, the use of welded or expanded columns had a significant impact on ultimate failure loads with the welded wire mesh showing a difference of nearly 28.10% from the expanded wire mesh. The analytical and experimental findings were well aligned [6]. The finite element approach was used to investigate the shear strength of a steel-concrete composite beam with angle connections at high temperatures [7]. The outcomes illustrated that the shear strength and slide, among other test results, were properly predicted by the finite element modelling. The maximum shear force error between analytical and laboratory values was found to be 21.6%, while the minimum shear force error in some samples was found to be very close to zero [7]. Concrete filled steel tube (CFST) columns have been emerging in structural applications because of the major advantages in their behaviour. The difficulties of local steel buckling, excessive concrete spalling, and the requirement to reduce formwork during construction in order to save construction costs have made the use of CFST columns necessary [8]. Contrary to normal RC columns, the steel tube in concrete-filled columns serves two purposes. It enhances the load-bearing, deformable, and seismic capabilities of RC columns and prevents the concrete cover from collapsing during an earthquake [8]. Fig. 1 depicts RCFST column and confinement by hoop reinforcement and steel tube.

Compared to RC columns, RCFST columns have additional benefits. Transverse reinforcement confines the concrete in a typical RC column but does not contain concrete cover, which will spall off in seismic events. The transverse reinforcement cannot prevent the longitudinal bars from buckling when the cover spalls off unless they are extremely and closely spaced [9]. A hollow steel tube (HST) shear connector of circular, square, and rectangular shapes indicated a 20% higher shear resistance with a longer width in the load direction for the rectangular HST in comparison with that in the smaller dimension. The energy absorption capacity values displayed 23% and 18% improvements with the

square HST rather than a headed shear stud when embedded in the concrete strengths of 25 MPa and 40 MPa, respectively [10].

Studies have shown that RCFST columns perform better than CFST columns in terms of toughness, load carrying capacity, and ductility [11, 12]. Moreover, a structure built with RCFST columns performs better against earthquakes than a comparable CFST structure [13]. In fact, it is possible to say that RCFST columns were created primarily to combine the benefits of RC columns with CFST columns. The earthquake response of RCFSTs with a shear span to depth ratio of one was examined and the steel tubes were found to be quite successful in avoiding shear failure in short columns [14]. Eight square RCFSTs with a shear span to depth ratio ranging from one to two were the subject of an investigation by Sakino et al. [15]. It was discovered that the confinement created by the steel tubes diminished as the ratio of width to thickness of tube and/or strength of concrete rose. The cyclic behaviour of three rectangular RCFST beam-columns were studied by Aboutaha et al. [16]. Their findings revealed that while confinement of a rectangular tube boosted columns' ductility, it had little impact on their flexural strength. In order to make a comparison, Zhang and Liu [17] studied the seismic response of four square RCFST beam-columns and compared with one normal RC column. The confinement of tube to concrete was demonstrated to increase the columns' ductility and flexural strength. A research work examined the seismic response of eight RCFST beam-columns including four square and four circular columns [18]. According to the test results, the RCFST beam-columns indicated outstanding ductility at high axial load ratios, and the circular RCFSTs provided superior ductility than the square RCFSTs. Furthermore, a study evaluated the behaviour and strength of tubed RC stub columns under axial compression [19]. The results illustrated that when the axial compression was applied to circular tube RC stub columns, the steel tube yielded at the peak load point; however, for square tube RC stub columns, the steel tube yielded at the post peak stage. In addition, for circular and square tube RC stub columns under the axial compression, ductility declined with an increase in the diameter/width to thickness ratio or compressive strength of concrete. Moreover, Wang et al. [20] conducted experimental research on the behaviour of eccentrically loaded short circular RCFST columns. The findings displayed that the average confining stress in the columns with low eccentricity was comparable to that in the columns exposed to axial load at the peak load. A comparison of CFSTs was made in an experimental study on the behaviour of axially compressed spirally reinforced CFST columns [21]. A spirally reinforced CFST column showed noticeably better post-yield behaviour than a CFST column. Besides, a reduction in the pitch spacing rate considerably enhanced the
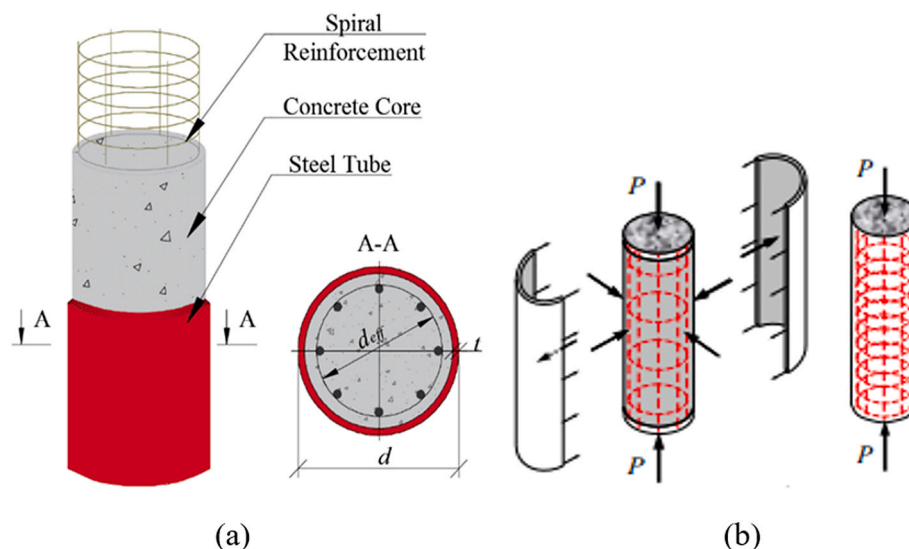

Fig. 1. (a) RCFST column; (b) Confinement by hoop reinforcement and steel tube [8].

post-yield behaviour of the spirally reinforced CFSTs. Hasan et al. [22] studied the mechanical behaviour of CFST columns reinforced with steel reinforcing bars under axial compression. The results demonstrated that stiffened CFST specimens had fewer lateral distortions than reinforced CFST specimens. The reinforced CFST specimens could not be used effectively because early buckling in the steel tubes occurred. On the contrary, the stiffened CFST specimens were less ductile and had lower strength capabilities than the reinforced CFST specimens. Furthermore, the compression loading against end shortening curves of the CFSTs revealed that when the number of reinforcing bars and/or steel tube thickness increased, the strength capacity, ductility, stiffness, and toughness also improved. Besides, the specimens with thick tubes had the strength to eliminate the negative impacts of early local buckling and were suitable to meet the performance requirements of the CFST columns. Despite several studies on CFST and RCFST columns, machine learning (ML) modelling and nonlinear finite element simulation of RCFST columns under the axial compression still need appropriate experimental data. This is the rationale behind the current investigation.

Over the past few decades, ABAQUS and ANSYS have been increasingly popular for the finite element modelling of steel tube RC columns. As the material technology develops, engineering structures are increasingly using better construction materials like high-performance steel and concrete. Besides, the finite element analysis is commonly utilised to resolve design and research difficulties [23,24]. To account for the expansion of materials, new finite element models (FEMs) are required to improve the prediction accuracy.

The literature has documented a number of ML techniques that predict the ultimate load for structural elements made of composite materials, including CFST columns. For instance, a support vector machine (SVM) was engaged to predict the load capacity of CFST columns [25]. The outcomes indicated that SVM is a powerful replacement for theoretical and empirical formulations. A gene expression programming (GEP) and artificial neural network (ANN) were applied to predict the CFST columns' bearing capacity. The input variables included external diameter, concrete compressive strength, steel tensile yield stress, steel thickness, and sample length [26]. The findings illustrated that GEP exhibited better performance indexes than the ANN model. The ultimate load capacity of CFST short columns subjected to axial compression made of carbon fibre-reinforced plastic (CFRP) was predicted using several ML algorithms [27]. In comparison to ANN, SVM, linear regression (LR), K-nearest neighbour (KNN), random forest (RF), Ada-Boost, gradient boosted decision trees (GBDT), and light gradient building (LGB), XGBoost yielded the best prediction performance with an R^2 value of 0.9719.

There is a gap in the earlier studies due to the paucity of finite element and ML modellings of RCFST columns under axial compression loading. Besides, previous studies displayed a little or no application of combined RF, gradient boosting (GB), KNN, gaussian process regression (GPR), ANN, extreme learning machine (ELM), and emotional neural network (ENN) as the ML tools in the prediction of ultimate load of RCFST columns subjected to concentric loading. This is the rationale behind this study. In this research, FEMs were created for 26 columns in the ABAQUS software from the experimental data obtained from the reviewed literature [19–22]. In addition to these 26 FEMs of columns, 59 more FEMs of columns were created by changing some parameters and subjecting to axial compression. The considered parameters are the thickness of steel tubes, centre-centre spacing of transverse steel bar, and yield strength of outer steel tube. Additionally, 7 ML models (RF, GB, KNN, GPR, ANN, ELM, and ENN) were constructed with the database obtained from FEMs and with 7 input features to predict the ultimate load of CFST and RCFST columns subjected to axial compression. The main goal of this study is to examine how these 85 columns respond to axial compression while being affected by the aforementioned characteristics.

The research is important because it ensures that generated models can be used in the building and construction industry without any

theoretical examination. It applies the FEM and ML analysis and assesses the effects of various factors such as ratio of vertical rebar to yield strength, the ratio of lateral hoops to yield strength, the area of concrete core that is inside the steel tube, the strength of the concrete, the area of the steel tube, the yield strength of the steel tube, and the height of the columns on the output parameter (ultimate load) of RCFST columns under axial compression loading. The creation of ML tools and their utilisation in the building and construction industry, notably for predicting the ultimate loads of RCFST columns, have the potential to reduce the costs, time, and resources used to run experiments.

2. Research methodology

There were three phases in this research methodology. For the CFST and RCFST columns, 26 FEM models were created in Stage 1. These models were used to calculate the ultimate load as well as the behaviour of the CFST and RCFST columns during axial compression. Stage 2 produced an additional 59 FEM models for the CFST and RCFST columns by calculating factors for the output of each FEM model's best-fitting hyperbolic curve. The configurations of each FEM model and the accompanying ultimate load were then entered into a database. The ultimate load (target value) was predicted using several ML approaches in Stage 3 utilizing the ratio of the vertical rebar multiplied by its yield strength, ratio of the lateral hoop multiplied by its yield strength, area of the concrete core that is inside the steel tube, the concrete strength, area of the steel tube, the yield strength of the steel tube, and the columns' height as input variables. Each stage of the research is fully described in Sections 2.1 to 2.3. Fig. 2 depicts the research methodology in a graphic format.

2.1. Details of FEMs

As stated earlier, 26 FEMs were created from the experimental data provided by the reviewed literature [19–22]. From Hamidian et al. [21] data, 5 FEMs were created, the specimens CFT-1, CFT-2, and CFT-3 were created as the first FEM specimen and named as S1; S45–1, S45–2, and S45-3 were created as the second FEM specimen and named as S2; S35–1, S35–2, and S35-3 were created as the third FEM specimen and named as S3; S25–1, S25–2, and S25-3 were created as the fourth FEM specimen and named as S4; and S15–1, S15–2, and S15-3 were created as the fifth FEM specimen and named as S5. From Hasan et al. [22] data, 14 FEMs were created and named as S6–S19. From Wang et al. [20] data, 2 FEMs were created and named as S20 and S21. From Liu et al. [19] data, 5 FEMs were created and named as S22–S26. The specimens, materials details, and FEM labels are presented in Table 1 [19–22]. From Table 1, $f_c^{'}$ represents the concrete's compressive strength; D, t, and f_y represent the diameter, thickness, and yield strength of the steel tube; d_b and n represent the diameter and number of the longitudinal steel bars; d_p and c_p represent the diameter and centre to centre spacing of the transverse steel bars, and s_p is the clear pitch spacing.

As mentioned earlier, in addition to these 26 FEM columns (S1–S26), 59 more FEM columns (S27–S85) were simulated, and the details are given in Table 2.

2.2. Modelling of FEMs

2.2.1. Modelling of mesh size and steel rebar

After the mesh sensitivity analysis, the calibrated and default plasticity values and mesh sizes employed in this study were the shape factor of 0.67 (default) and the viscosity parameter of 0.0005.. A convergence problem was addressed by calibrating the viscosity parameter. For the concrete, steel tube, and steel rebar, the mesh sizes of 25, 34, and 15 mm were used, respectively [28]. The density of 7850 kg/m³, Young's modulus of 200000 MPa, and Poisson's ratio of 0.3 were utilised for the steel rebars[29]. The stress-strain relation was obtained by using Ramberg-Osgood, as expressed in Equation (1) [30], and the
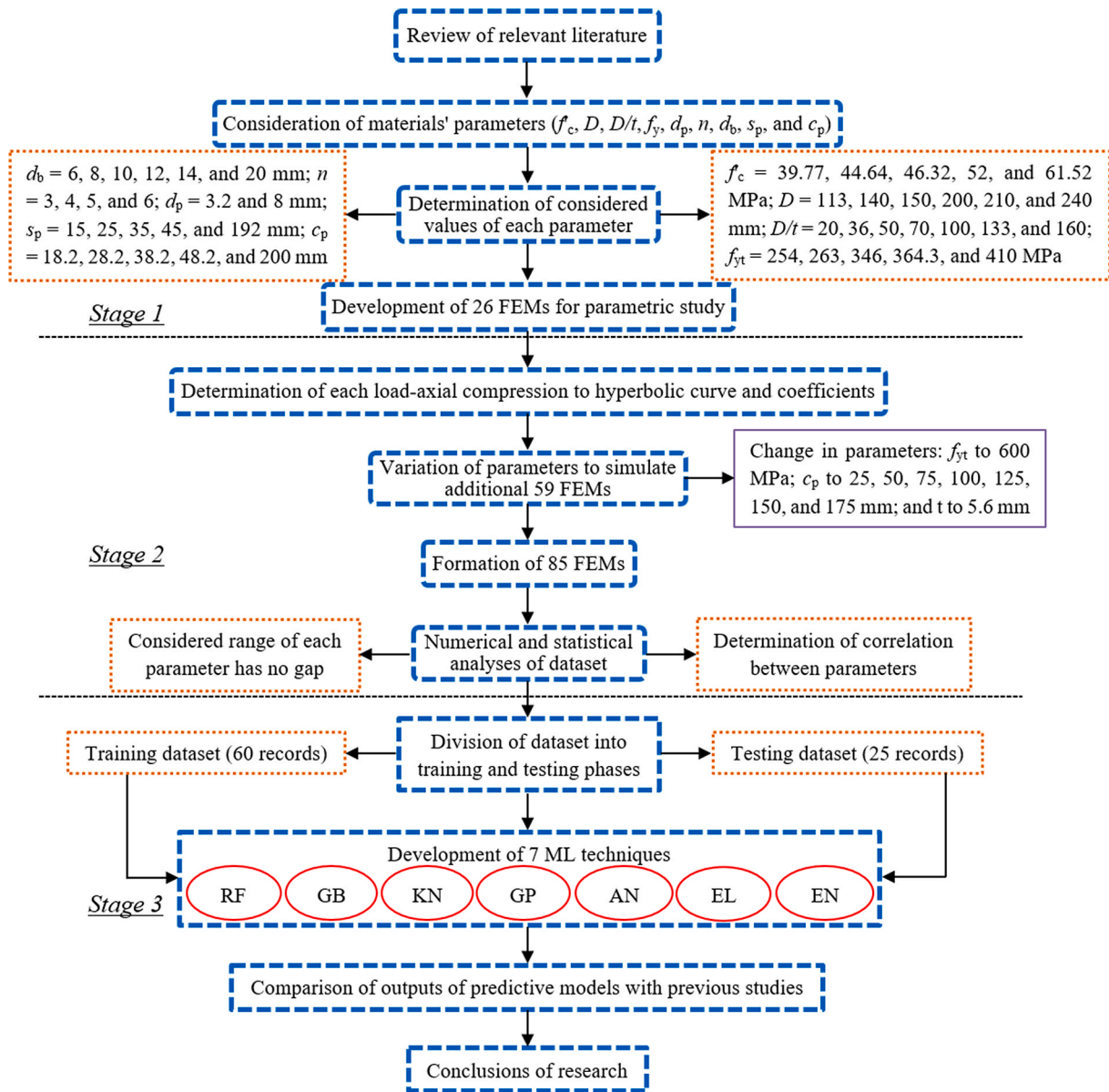
Fig. 2. Flowchart showing research methodology.

stress-strain curve is depicted in Fig. 3. The elongation of the steel rebar was determined with the help of the model suggested by Tao et al. [31].

$$\varepsilon = \frac{\sigma}{E} + 0.002\left(\frac{\sigma}{F_{ty}}\right)^{n} \quad (1)$$

2.2.2. Modelling of loading plates and steel tube

The density of 7850 kg/m³, Young's modulus values of 300000 MPa and 200000 MPa, and Poisson's ratios of 0.00001 and 0.3 were respectively used for the loading plates and steel tube in accordance with the relevant studies [29,32]. The stress-strain relation of the steel tube was determined with the help of the model suggested by Tao et al. [31].

2.2.3. Modelling of concrete

For example, the density, Young's modulus, and Poisson's ratio of M52 grade concrete were taken as 2400 kg/m³, 34108.515 MPa, and 0.2, respectively [32–36]. When a CFST column is compressed axially, the steel tube confines the concrete core's lateral expansion. The concretes' ductility and strength can be improved by this passive

confinement. The process between concrete and steel tube is called "composite action" and is widely engaged [37]. It is believed that when two components interact, the constrained concrete enters a triaxial condition and the steel enters a biaxial stress state. Therefore, to model this behaviour, the concrete damaged plasticity (CDP) model was employed in ABAQUS. The key material characteristics for this model included the ratio of the second stress invariant on the tensile meridian to that on the compressive meridian (K_c), the dilation angle (ψ) illustrated in Equation (2), flow potential eccentricity (e), modulus of elasticity (E_c), ratio of compressive strength under biaxial loading to uniaxial compressive strength (f_{bo}/f'_c), viscosity parameter, and stress-strain relation of concrete under compression and tension. Therefore, the effects of f_{bo}/f'_c, K_c, and ψ on the load-axial compression curve based on the sensitivity analysis are indicated in Fig. 4 (a), (b), and (c), respectively.

$$\psi = 25.331\xi_s^{-0.345} \quad (2)$$

ξ_s is the confinement factor and can be determined using Equation (3):

Table 1
Specimens, materials details, and FEMs labels.

No.	Specimen label	FEM label	$f_c^{'}$ (MPa)	Properties of steel tube			Properties of longitudinal steel bar		Properties of transverse steel bar		
				D (mm)	D/t	f_y (MPa)	d_b (mm)	n	d_p (mm)	s_p (mm)	c_p (mm)
1	CFT-1 CFT-2 CFT-3	S1	52	140	50	355	–	–	–	–	–
2	S45-1 S45-2 S45-3	S2	52	140	50	355	6	6	3.2	45	48.2
3	S35-1 S35-2 S35-3	S3	52	140	50	355	6	6	3.2	35	38.2
4	S25-1 S25-2 S25-3	S4	52	140	50	355	6	6	3.2	25	28.2
5	S15-1 S15-2 S15-3	S5	52	140	50	355	6	6	3.2	15	18.2
6	C-1	S6	39.77	113	36	460	–	–	–	–	–
7	1-3-8-W	S7	39.77	113	36	460	8	3	–	–	–
8	1-3-12-W	S8	39.77	113	36	460	12	3	–	–	–
9	1-4-8-W	S9	39.77	113	36	460	8	4	–	–	–
10	1-4-12-W	S10	39.77	113	36	460	12	4	–	–	–
11	1-6-8-W	S11	39.77	113	36	460	8	6	–	–	–
12	1-6-12-W	S12	39.77	113	36	460	12	6	–	–	–
13	C-2	S13	39.77	113	20	410	–	–	–	–	–
14	2-3-8-W	S14	39.77	113	20	410	8	3	–	–	–
15	2-3-12-W	S15	39.77	113	20	410	12	3	–	–	–
16	2-4-8-W	S16	39.77	113	20	410	8	4	–	–	–
17	2-4-12-W	S17	39.77	113	20	410	12	4	–	–	–
18	2-6-8-W	S18	39.77	113	20	410	8	6	–	–	–
19	2-6-12-W	S19	39.77	113	20	410	12	6	–	–	–
20	c-200-0-1 c-200-0-2 c-200-0-3	S20	44.64	200	133	364.3	20	6	8	192	200
21	c-240-0-1 c-240-0-2 c-240-0-3	S21	44.64	240	160	364.3	20	6	8	192	200
22	c-150-3-80-a-235	S22	61.52	150	50	254	10	4	–	–	–
23	c-210-3-80-a-235	S23	61.52	210	70	254	14	4	–	–	–
24	c-200-2-80-a-235	S24	61.52	200	100	263	12	5	–	–	–
25	c-210-3-50-a-235	S25	46.32	210	70	254	14	4	–	–	–
26	c-210-3-80-a-345	S26	61.52	210	70	346	14	4	–	–	–

$$\xi_s = \frac{A_s f_y}{A_c f_c^{'}} \qquad (3)$$

where A_c and A_s are the cross-sectional areas of the concrete and steel tube, respectively, and f_y is the steel yield strength and $f_c^{'}$ is the concretes' cylinder compressive strength. In this study a new relation for determining the parameter (K_c) is given in Equation (4) as:

$$K_c = -0.019 \ln(f_c^{'}) + 0.7891 \qquad (4)$$

Modulus of elasticity (E_c) can be calculated utilising Equation (5) [38]:

$$E_c = 4730\sqrt{f_c^{'}} \qquad (5)$$

$f_{b0}/f_c^{'}$ can be calculated using Equation (6) [39]:

$$\frac{f_{bo}}{f_c^{'}} = 1.5(f_c^{'})^{-0.075} \qquad (6)$$

The viscosity parameter and flow potential eccentricity (e) were set to 0 and 0.1, respectively [31]. Fig. 5 shows the stress-strain relationship of the concrete under compression for FEM S1. A new 3-stage model was used to represent the stress-strain relation of the concrete under compression demonstrated in Fig. 5. There is minimal to no interaction between the concrete and steel tube in the early stage, i.e., from point O to point A (Fig. 5). Therefore, up until the peak strength $f_c^{'}$ is achieved, the

ascending branch of the stress-strain relationship of the unconfined concrete is suitable to be utilized to depict the OA curve. After that, the increased peak strain of the concrete from confinement is represented as a plateau, i.e., from point A to point B. At this stage, any increase in the strength of the concrete from confinement is represented in simulation by the concrete and tube interaction. A softening region with the increased ductility due to confinement is specified beyond point B.

The ascending curve, OA, is obtained by a model and is presented in Equation (7) [40]:

$$\sigma = \frac{xr}{r - 1 + x^r} f_c^{'} \qquad (7)$$

where

$$x = \frac{\varepsilon}{\varepsilon_{co}} \qquad (8)$$

The strain at peak stress under uniaxial compression (ε_{co}) and the secant modulus of concrete are calculated using Equations 9–11 [41]:

$$\varepsilon_{co} = 0.00076 + \sqrt{(0.626 f_c^{'} - 4.33) \times 10^{-7}} \qquad (9)$$

$$r = \frac{E_c}{E_c - E_{sec}} \qquad (10)$$

$$E_{sec} = \frac{f_c^{'}}{\varepsilon_{co}} \qquad (11)$$

Table 2
Details of FEMs S27–S85.

| No.	FEM label	Similar to	Changed parameter
1	S27	S1	f_y changed to 600 MPa
2	S28	S2	f_y changed to 600 MPa
3	S29	S3	f_y changed to 600 MPa
4	S30	S4	f_y changed to 600 MPa
5	S31	S5	f_y changed to 600 MPa
6	S32	S6	f_y changed to 600 MPa
7	S33	S7	f_y changed to 600 MPa
8	S34	S8	f_y changed to 600 MPa
9	S35	S9	f_y changed to 600 MPa
10	S36	S10	f_y changed to 600 MPa
11	S37	S11	f_y changed to 600 MPa
12	S38	S12	f_y changed to 600 MPa
13	S39	S13	f_y changed to 600 MPa
14	S40	S14	f_y changed to 600 MPa
15	S41	S15	f_y changed to 600 MPa
16	S42	S16	f_y changed to 600 MPa
17	S43	S17	f_y changed to 600 MPa
18	S44	S18	f_y changed to 600 MPa
19	S45	S19	f_y changed to 600 MPa
20	S46	S20	f_y changed to 600 MPa
21	S47	S21	f_y changed to 600 MPa
22	S48	S22	f_y changed to 600 MPa
23	S49	S23	f_y changed to 600 MPa
24	S50	S24	f_y changed to 600 MPa
25	S51	S25	f_y changed to 600 MPa
26	S52	S26	f_y changed to 600 MPa
27	S53	S20	c_p changed to 25 mm
28	S54	S21	c_p changed to 25 mm
29	S55	S20	c_p changed to 50 mm
30	S56	S21	c_p changed to 50 mm
31	S57	S20	c_p changed to 75 mm
32	S58	S21	c_p changed to 75 mm
33	S59	S20	c_p changed to 100 mm
34	S60	S21	c_p changed to 100 mm
35	S61	S20	c_p changed to 125 mm
36	S62	S21	c_p changed to 125 mm
37	S63	S20	c_p changed to 150 mm
38	S64	S21	c_p changed to 150 mm
39	S65	S20	c_p changed to 175 mm
40	S66	S21	c_p changed to 175 mm
41	S67	S46	c_p changed to 25 mm
42	S68	S47	c_p changed to 25 mm
43	S69	S46	c_p changed to 50 mm
44	S70	S47	c_p changed to 50 mm
45	S71	S46	c_p changed to 75 mm
46	S72	S47	c_p changed to 75 mm
47	S73	S46	c_p changed to 100 mm
48	S74	S47	c_p changed to 100 mm
49	S75	S46	c_p changed to 125 mm
50	S76	S47	c_p changed to 125 mm
51	S77	S46	c_p changed to 150 mm
52	S78	S47	c_p changed to 150 mm
53	S79	S46	c_p changed to 175 mm
54	S80	S47	c_p changed to 175 mm
55	S81	S1	t changed to 5.6
56	S82	S2	t changed to 5.6
57	S83	S3	t changed to 5.6
58	S84	S4	t changed to 5.6
59	S85	S5	t changed to 5.6
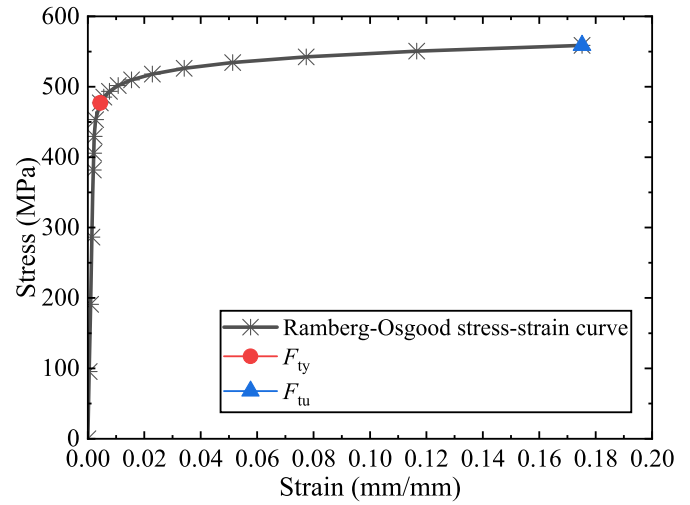
Fig. 3. Stress-strain curve of steel rebar.

displays the stress-strain relationship of concrete under tension for FEM S1.

$$\sigma = f_r + (f_c' - f_r)exp\left[-\left(\frac{\varepsilon - \varepsilon_{cc}}{\alpha}\right)^\beta\right] \quad \varepsilon \geq \varepsilon_{cc} \tag{14}$$

where

$$f_r = 0.7\left(1 - e^{-1.38\xi_s}\right)f_c' \leq 0.25f_c' \tag{15}$$

$$\alpha = 0.04 - \frac{0.036}{1 + e^{6.08\xi_s - 3.49}} \tag{16}$$

Fig. 6 was obtained using Equation (17) [43]:

$$\sigma_t = f_t\left(\frac{\varepsilon_{ct}'}{\varepsilon}\right)^{0.85} \tag{17}$$

where

$$\varepsilon_{ct}' = \frac{f_t}{E_c} \tag{18}$$

$$f_t = 0.26(1.25f_c')^{2/3} \tag{19}$$

2.2.4. Details of FEM structure

The element used to model the concrete and loading plates was solid homogenous. Truss element was utilised to model the reinforcing rebars including vertical and spirals, while shell element was used for the steel tube. The thickness integration points for the steel tube were nine, and the thickness integration rule used was Simpson. Because the steel tube acts as a shell element and does not carry compression loads, the diameter of the loading plates was maintained at the same level as the diameter of the concrete. As a result, we did not make the loading plates attached to the steel tube, as depicted in Fig. 7.

The element shape for mesh controls of the concrete and loading plate was hex, technique was sweep, and algorithm was advancing front. The element shape for mesh controls of the steel tube was quad and technique was sweep. The mesh size of the concrete, loading plate, and steel tube was approximately equal to D/15. The mesh size of the spirals and vertical rebars was taken approximately double 2D/15. The element type of the concrete and loading plates was 3D Stress "C3D8R: an 8-node linear brick, reduced integration, hourglass control". The element type of the steel tube was Shell "S4R: a 4-node doubly curved thin or thick shell, reduced integration, hourglass control, finite membrane strains". The element type of the spirals was Truss "T3D2: a 2-node linear 3-D truss". The element type of the vertical rebars was Truss "T3D2: a 2-

The strain at B (ε_{cc}) can be determined employing Equation (12) [40]:

$$\frac{\varepsilon_{cc}}{\varepsilon_{co}} = e^k, k = \left(2.9224 - 0.00367f_c'\right)\left(\frac{f_B}{f_c'}\right)^{0.3124+0.002f_c'} \tag{12}$$

$$f_B = \frac{(1 + 0.027f_y)e^{-0.02\frac{D}{t}}}{1 + 1.6e^{-10}(f_c')^{4.8}} \tag{13}$$

According to a relevant research work, an exponential function was utilized for the descending branch of the concrete model BC (Fig. 5) [42]. This is illustrated in Equation (14), and β is taken as 1.2 [31]. Fig. 6
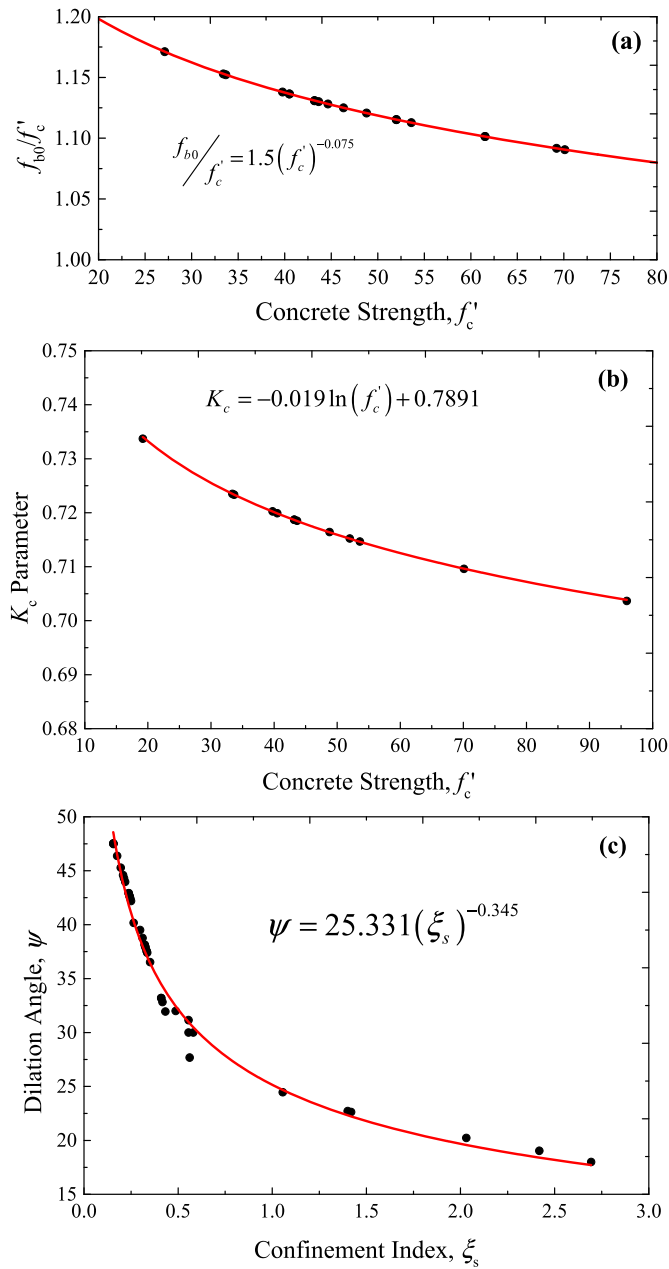
$$\frac{f_{b0}}{f_c'} = 1.5\left(f_c'\right)^{-0.075}$$

(a)

$$K_c = -0.019\ln\left(f_c'\right) + 0.7891$$

(b)

$$\psi = 25.331\left(\xi_s\right)^{-0.345}$$

(c)

Fig. 4. Relationship between: (a) f_{b0}/f_c' vs. f_c', (b) K_c vs. f_c', and (c) ψ vs. ξ_s.

Fig. 5. Stress-strain curve of concrete under compression.

$$\sigma_t = f_t\left(\frac{\epsilon_{ct}'}{\epsilon}\right)^{0.85}$$

$$\epsilon_{ct}' = \frac{f_t}{E_c}$$

Fig. 6. Stress-strain curve of concrete under tension.
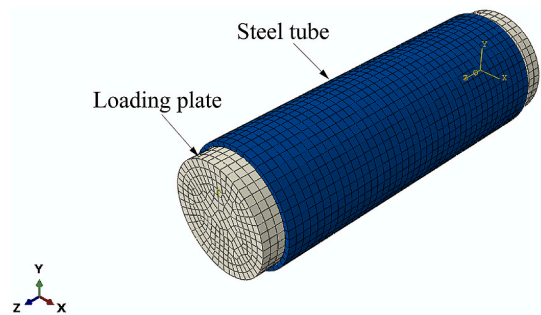
Fig. 7. Connection between loading plate and steel tube.

node linear 3-D truss".

In the interaction among the steel tube, loading plates, and concrete, the steel tube and loading plates were the master surface, and the concrete was the slave surface. In the interaction, the tangential and normal behaviours were considered, and the friction coefficient was 0.6. In the interaction between the vertical rebar, spirals, and concrete, the embedded region was considered as the steel reinforcement and the host region was considered as the whole model including the concrete part. In the interaction between the vertical rebar and spirals, the tie constraint was used between the vertical rebars and the spirals considering the surface region of the two materials to be tied. The loads were directly applied on the top and bottom loading plates. The top plate was fixed from translation and rotation except the translation in the Z-axis. The bottom surface was fixed against translation as well as rotation, aspresented in Fig. 8.

In loading, the step was static general, and the nonlinear deformation was set on. In the step, automatic stabilization was employed, and the
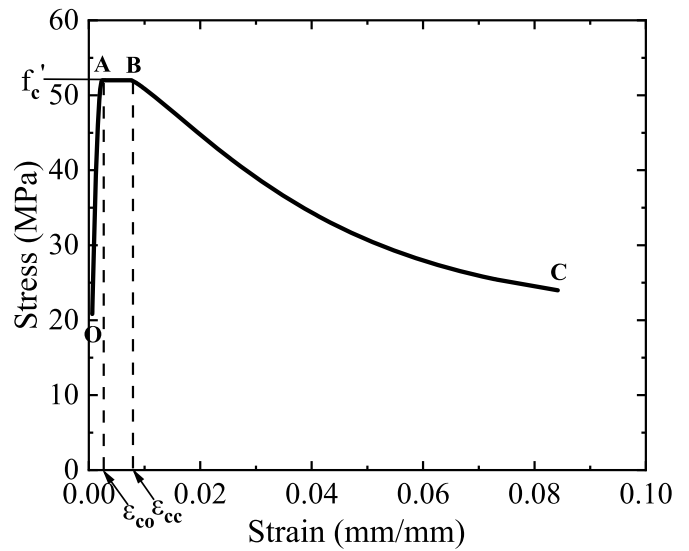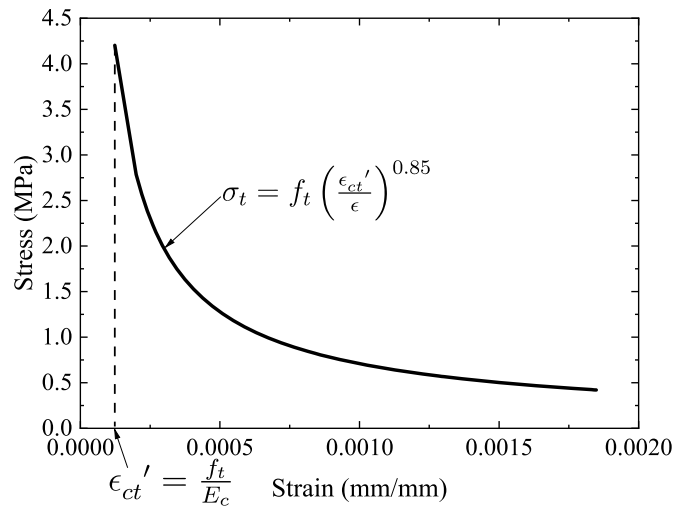
dissipated energy fraction was specified as 0.0002. In addition, adaptive stabilization with a maximum ratio of stabilization to strain energy of 0.05 was used. For the incrementation of the steps, automatic type was selected, and the maximum number of increments was 10000. The initial increment size was 0.05, and the minimum and maximum increment sizes were 0.00000001 and 0.1, respectively.
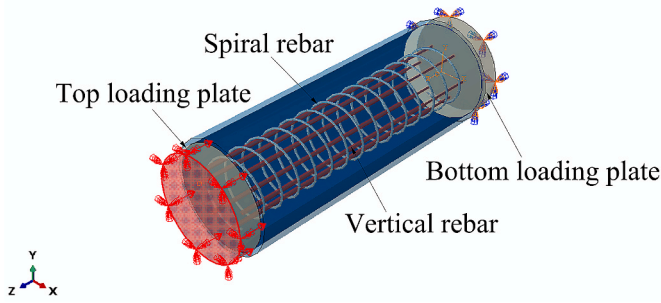
Fig. 8. Boundary conditions of top and bottom loading plates.

2.3. Assessment of FEM with test specimens

After modelling, FEMs (S1–S26) were subjected to axial compression as prescribed in the literature [19–22]. Fig. 9 shows the relationship between the load applied on FEMs and the load applied on the test specimens. According to Fig. 9, the finite element modelling analysis can predict the experimental loads of RCFST columns at 98.90% confidence and predictive intervals, indicating a strong relationship. The axial load versus axial displacement curves of these FEMs were compared with the outcomes of the experimental tests following the application of axial compression, and the results are shown in Fig. 10. Fig. 10 demonstrates that the results of the experimental tests and FEMs are correlated.

2.4. ML models

2.4.1. Data processing and analysis

The input parameters are the ratio of the longitudinal steel bar multiplied by its yield strength (input 1), ratio of the lateral hoop multiplied by its yield strength (input 2), area of the concrete core that is inside the steel tube (input 3), the concrete strength (input 4), area of the steel tube (input 5), the yield strength of the steel tube (input 6), and height of columns (input 7). The descriptive statistics of the input parameters and output parameter (ultimate load) are listed in Table 3. The results can be seen to represent a wide variety of experimental datasets. When all the parameters were analysed, as indicated by Pearson correlation in Fig. 11, the correlation among the output and parameters (inputs 3 and 7) were greater than other parameters. In contrast, it was discovered that there is a negative association between input 5 and output (ultimate load). This discrepancy may be explained by the materials' properties and constitutive behaviour in the theoretical model, which differed from the actual values.
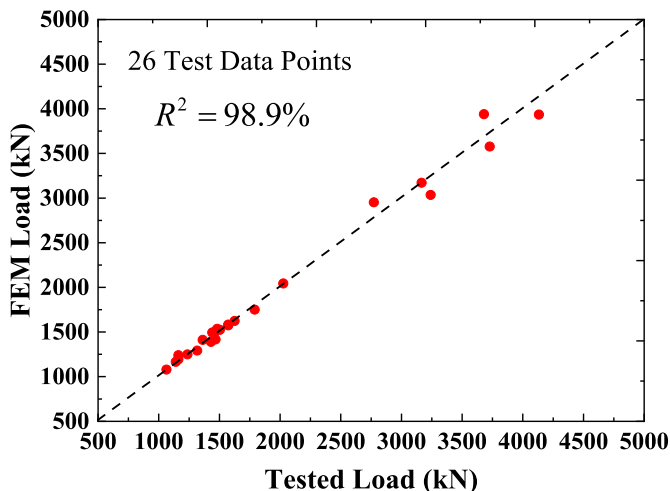

Fig. 9. FEM loads vs. tested loads.

2.4.2. Used learning techniques

a. RF. For the classification and regression applications, the most advanced ensemble learning methodologies are the RF and GB algorithms. An ensemble learning strategy combines predictions from different ML algorithms, often known as base learners, to produce predictions that are more accurate. A technique called RF creates numerous decision trees concurrently. These trees serve as the RF's foundational learners, and each tree is constructed using an independent bootstrap sample of the entire data set. This process is known as bagging. A specific number of variables is chosen at random from each node to serve as candidate for each split. Then, from among this random collection of variables, the optimal split point is chosen. This method is referred to as feature sampling. Before the forest grows, the number of variables is fixed. The trees in RF are completely developed (no pruning step), in contrast to the categorisation and regression trees of previous studies [44,45]. Feature sampling and bagging are the basic principles of RF. There are two randomizing processes that make sure the trees are distinct from one another and have lower correlations. The final forecast of a RF regressor is determined by averaging the results of all the separate trees, while in classification, the majority rule is applied. The number of trees and number of randomly selected variables at each split when generating the trees are the two most crucial RF hyper parameters [46,47].

b. GB. GB sequentially trains a large number of weak learners to produce a precise estimation of response variable. A ML model is considered a weak learner if its performance is barely above the chance. The shallow decision trees in the case of GB trees are the weak learners. The ensemble model's loss function is reduced by adding each subsequent tree to the model, which is a combination of all prior trees. The loss function, which user can select, is dependent on the nature of the task being performed. The squared loss is the usual selection for regression. By following the gradient of the overall loss function, trees that minimize the loss function are sequentially added, resulting in a decrease in the total prediction error. In previous studies, GB trees were described in detail that was more technical [45,48]. The GB trees have a large number of hyper parameters that must be adjusted in order to achieve optimal performance. Some of these hyper parameters govern the GB procedure itself, such as the number of trees and the learning rate, while others govern the tree-building procedure itself, such as the minimum node size, the dataset sample, and the maximum depth [49,50].

c. KNN. Finding the k items in the training dataset that are most similar to the data object being tested is the difficult ML technique known as KNN [75]. The datasets were normalised using Euclidean distance to overcome this issue. Labels are given based on the frequency of a particular class in this location. The number of neighbours is represented by small positive integer k. Euclidean distance, also known as standardised Euclidean distance, is calculated using standardised data in the KNN technique. This measurement of distance is provided in Equation (20):

$$D_{x,y} = \sqrt{\sum_{n=1}^{N} \frac{1}{S_n^2}(x_n - y_n)^2} \tag{20}$$

Two n-dimensional vectors are compared using the standardised Euclidean distance, where s_n stands for sample standard deviation of nth variable. In this investigation, best result was chosen for the prediction purpose after testing the 1 to 10 (k = 1, 2, …,10) nearest neighbours.

d. GPR. GPR is a probabilistic regression framework that models random variables as gaussian distributions. GPR predicts outcomes based on the mean and covariance functions of input features. It assumes stationary and additive noise that follows a gaussian distribution. The
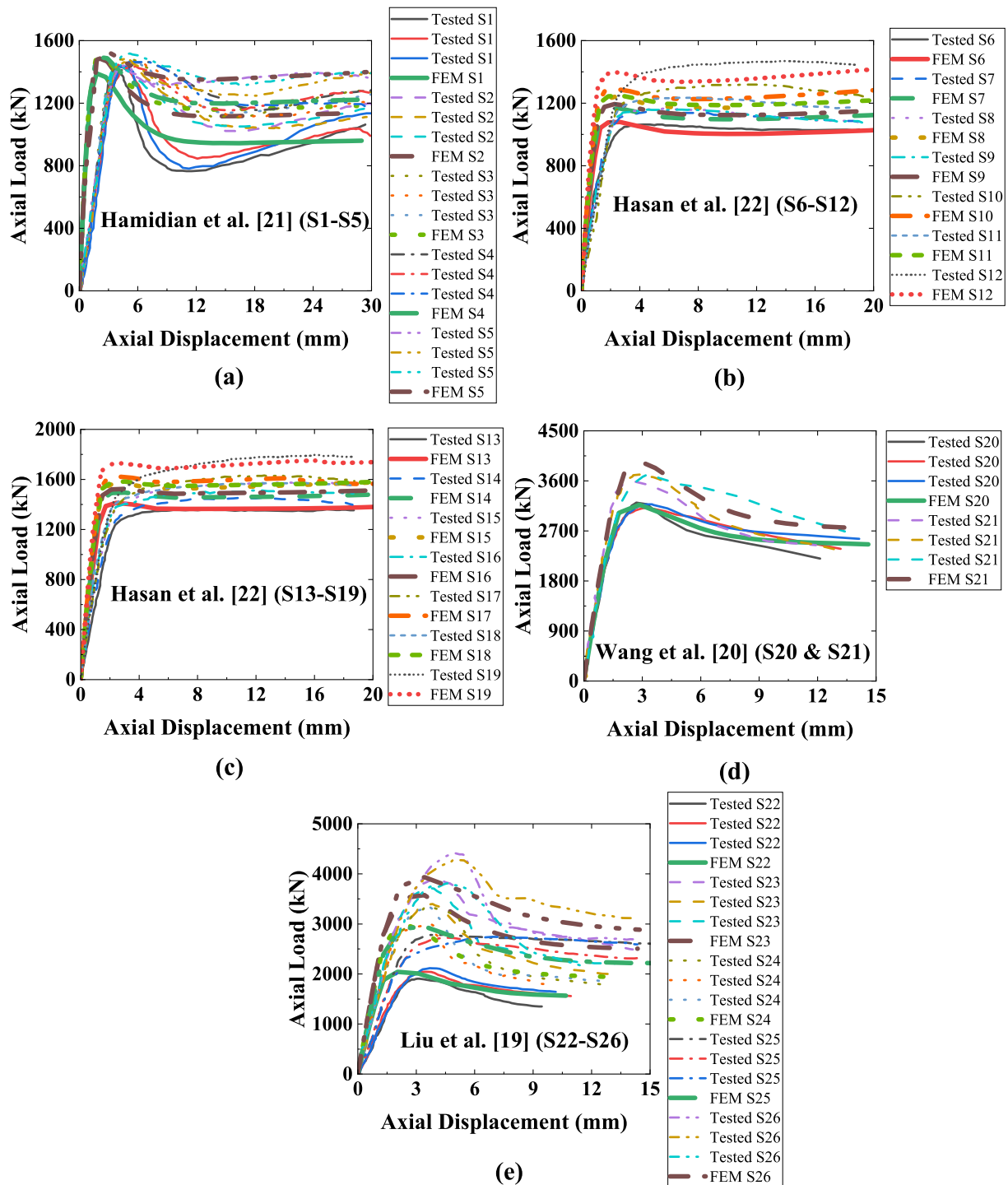
Fig. 10. Comparison of axial load against axial displacement curves of experimental results and FEMs for: (a) S1–S5, (b) S6–S12, (c) S13–S19, (d) S20 and S21, and (e) S22–S26.

GPR model uses input values and a latent variable to calculate output. The advantages of GPR include its ability to interpolate and its prior gaussian assumption. The mean function is utilised in cases of missing or unobserved input space, while the covariance function determines the correlation between inputs. Hyper-parameters are employed to define the maximum allowable covariance, the decay in correlation with distance, and the unknown variance. These hyper-parameters are grouped together as a random realisation vector and are used for predictions [51–54].

e. ANN. ANN is frequently employed to address limitations of traditional algorithms when handling complicated issues. By creating an input-output mapping for simulations, ANN can gain hidden information from the supplied data samples without having a precise mathematical explanation of the underlying process to be addressed. There is a plethora of distinct ANN variation kinds in the earlier literature [55–59]. This research chooses to use a feed-forward network trained with back-propagation. The input layer receives the external signal; hidden layer processes the data in an orderly manner, and output layer exports result. These three types of layers are frequently present in feed-forward

Table 3
Statistical descriptive of input and output parameters.

| Parameter	Maximum	Minimum	Std. Dev.	Variance	Mean	Median	Mode	Skewness	Kurtosis
Input 1	39.54	0	10.87	118.30	15.86	17.70	29.51	0.261	−0.997
Input 2	12.765	0	2.70	7.31	1.75	0	0	2.11	4.994
Input 3	44132.79	8069.12	13389.63	179282297.40	21073.2	14192.64	9012.46	0.571	−1.223
Input 4	61.52	39.77	6.94	48.21	45.99	44.64	39.77	1.079	0.164
Input 5	2365.44	935.78	426.76	182130.5	1379.15	1207.36	1091.47	0.831	−0.754
Input 6	600	254	117.04	13698.77	457.69	410	600	0.084	−1.393
Input 7	720	258.98	179.60	32257.02	452.03	400	260.82	0.226	−1.573
Output	6091.23	1063.5	1223.31	1496500	2533.43	1961.45	1161.9	0.656	−0.726
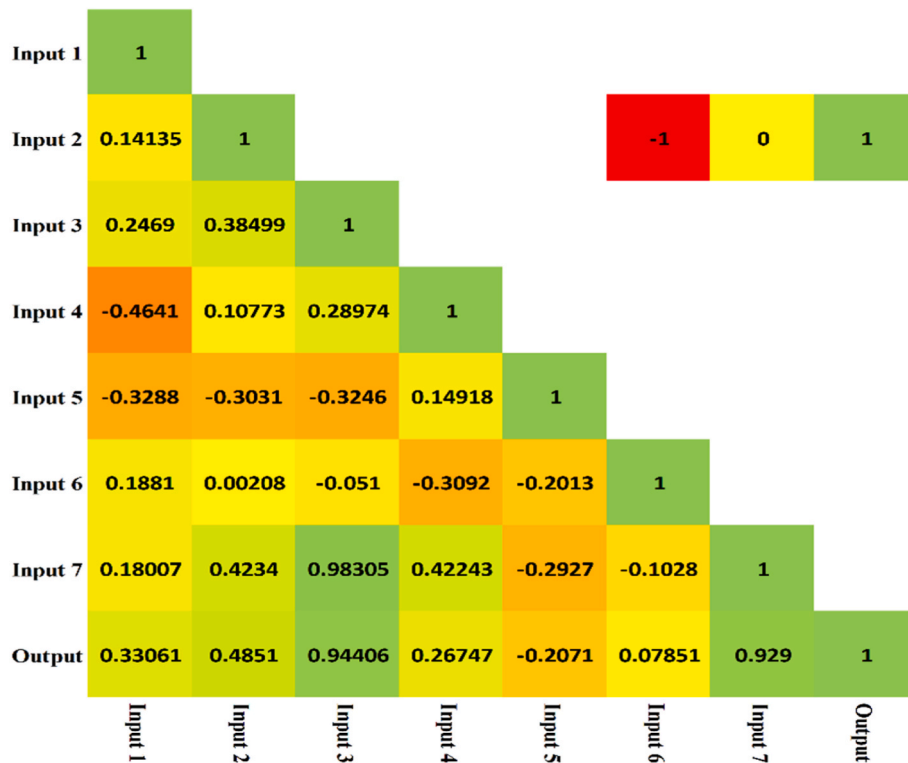
Fig. 11. Pearson correlation with heat map.

ANN. A feed-forward artificial neural network (FFANN) training process involves two essential steps [60,61]. In first method, from input layer, data are transmitted forward through the hidden layers to the output layer. The second method is the reverse method, which distributes the derivatives of objective function with respect to the weights among all the network nodes. Based on the discrepancy between goal outputs and network's simulated outputs, weights and biases are dynamically adjusted. Each node in a layer using a transfer function, producing an accumulated result that is then transmitted to the following layer, computes the inner product of weight vector and input vector. While connections between neurons in the same layer do not occur, rather all the neurons in the following layer are connected to the neurons in the layer before.

f. ELM. Since the FFANN approach's back-propagation learning involves a lot of processing work, the ELM technique has been used to address this. Huang et al. [62] provided a detailed mathematical proof of ELM. In contrast to the gradient-based iterative neural network technique, the single step learning process in ELM is achieved through non-iterative tuning of hidden neurons. In order to make ELM comparably faster than ANN-based backpropagation learning approaches, Moore-Penrose generalised inverse is applied [63]. The ELM learning method operates in 3 steps if the training set $\{(x_i, t_i) | x_i \in R^d, t_i \in R^m, i =$

$1, 2, \ldots, n\}$, as well as the activation function G and hidden unit number n' are provided. The hidden unit parameters $\{(a_i, b_i), i = 1, 2, \ldots, n'\}$ are assigned at random in the first phase with i equals 1 to n'. During the second stage of the method, the output matrix H (Equation (21)) of the hidden layer is generated. Output weight β is determined in third step. In order to find a non-linear relationship among inputs and outputs, the ELM learning algorithm used in the current study made use of the radial basis activation function: 15 hidden neurons, 1 output neuron, and 7 input neurons make up the final structure of ELM.

$$\left\{ H = \begin{bmatrix} h_{(x_1)} \\ h_{(x_2)} \\ \vdots \\ h_{(x_n)} \end{bmatrix} \right\} \tag{21}$$

.

g. ENN. ENN has improved the traditional feedforward neural network (FFNN). In ENN, the network's performance is enhanced by using an emotional system to modify the neuron's operation rather than the synthetic hormones utilised in the conventional FFNN. The i_{th} output neuron can be quantitatively described as per Equation (22) when the

hormonal glands H_a, H_b, and H_c are considered as dynamic coefficients [64–66].

2.4.3. Computation of performance indicators

The computation of the models' performance was done by consid-

$$Y_i = \underbrace{\left(\rho_i + \sum_h \theta_{i,h} H_h\right)}_{1} \times f\left(\sum_j \underbrace{\left(\alpha_i + \sum_h \psi_{i,h} H_h\right)}_{2} \times \underbrace{\left(\beta_{i,j} + \sum_h \varphi_{i,j,k} H_h\right)}_{3} X_{ij}\right) + \underbrace{\left(\lambda_i + \sum_h \varphi_{i,h} H_h\right)}_{4} + \underbrace{\left(\delta_i + \sum_h \rho_{i,h} H_h\right)}_{5} \tag{22}$$

where, i = input, h = hidden, j = output, and f = transfer function.

Equations (23) and (24) were employed to evaluate and enforce the model hormone values (H_h) on the neuron network, as proposed by Nourani [65].

$$H_h = \sum_i H_{i,h}, (h = a, b, c) \tag{23}$$

$$H_{i,h} = glandity_{i,h} \times Y_i \tag{24}$$

ering two statistical parameters. These parameters are coefficient of determination (R^2), and root mean square error (RMSE) given in Equations (25) and (26), respectively. The ideal value of R^2 is 1 and RMSE is zero.

$$R^2 = \frac{\sum_{i=1}^{n}(y_i - y_{mean})^2 - \sum_{i=1}^{n}(y_i - \widehat{y}_i)^2}{\sum_{i=1}^{n}(y_i - y_{mean})^2} \tag{25}$$
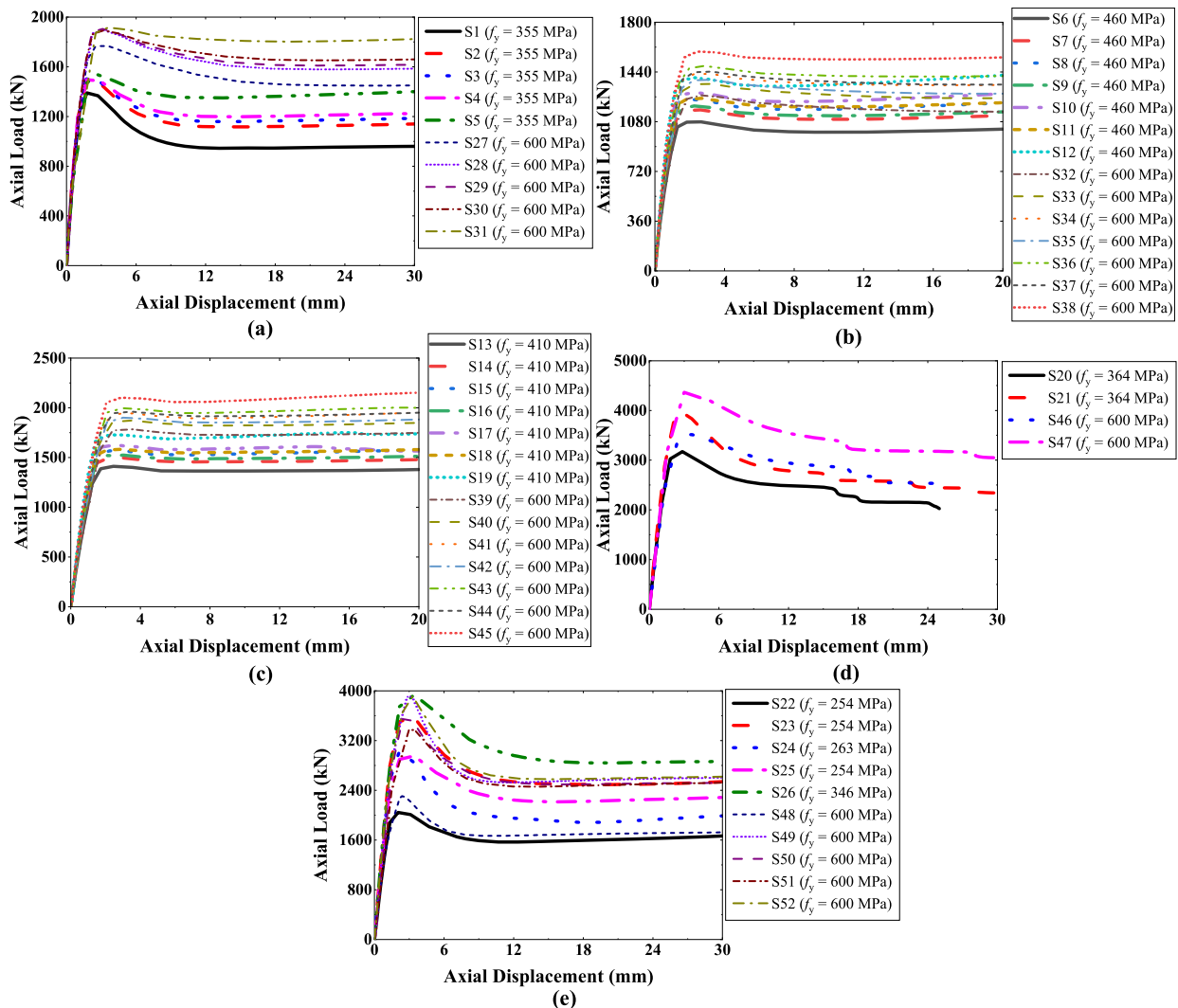

Fig. 12. Effect of steel tubes' yield strength on compression behaviour for: (a) S1–S5 and S27–S31, (b) S6–S12 and S32–S38, (c) S13–S19 and S39–S45, (d) S20, S21, S46, and S47, and (e) S22–S26 and S48–S52.

$$RMSE = \sqrt{\frac{1}{N} \sum_{i=1}^{n} (y_i - \widehat{y}_i)^2} \tag{26}$$

where y_i and $\widehat{y}_i$ are the actual and predicted ith values, and N is number of the data sample.

3. Results and discussion

3.1. Effect of yield strength of steel tube

Fig. 12 illustrates the impact of the steel tubes' yield strength on the FEMs' performance under axial compression. From Fig. 12(a), it can be observed that FEM S1, whose steel tube has an yield strength of 355 MPa, has a compression capacity of 1390.04 kN, whereas FEM S27, whose steel tube has an yield strength of 600 MPa, has a compression capacity of 1766.95 kN. Similar to this, for FEMs S2, S3, S4, and S5, where the steel tubes' yield strength is 355 MPa, the compression capacities are 1493.99 kN, 1503.65 kN, 1495.97 kN, and 1535.81 kN, respectively, and for FEMs S28, S29, S30, and S31, where the steel tubes' yield strength increased to 600 MPa, the compression capacities are 1894.25 kN, 1905.14 kN, 1892.05 kN, and 1915.81 kN, respectively.

FEM S1 has an axial displacement of 1.7 mm at the compression capacity level, while FEM S27 exhibits additional ductility and has an axial displacement of 3.6 mm. At the same compression capacity level, FEMs S2, S3, S4, and S5 have an axial displacement of 1.7 mm, 1.7 mm, 1.7 mm, and 2.7 mm, respectively, while FEMs S28, S29, S30, and S31 have axial displacements of 3.2 mm, 3.1 mm, 3.2 mm, and 3.6 mm, respectively. Fig. 10 (b)–(e) display a similar pattern. Despite consistent
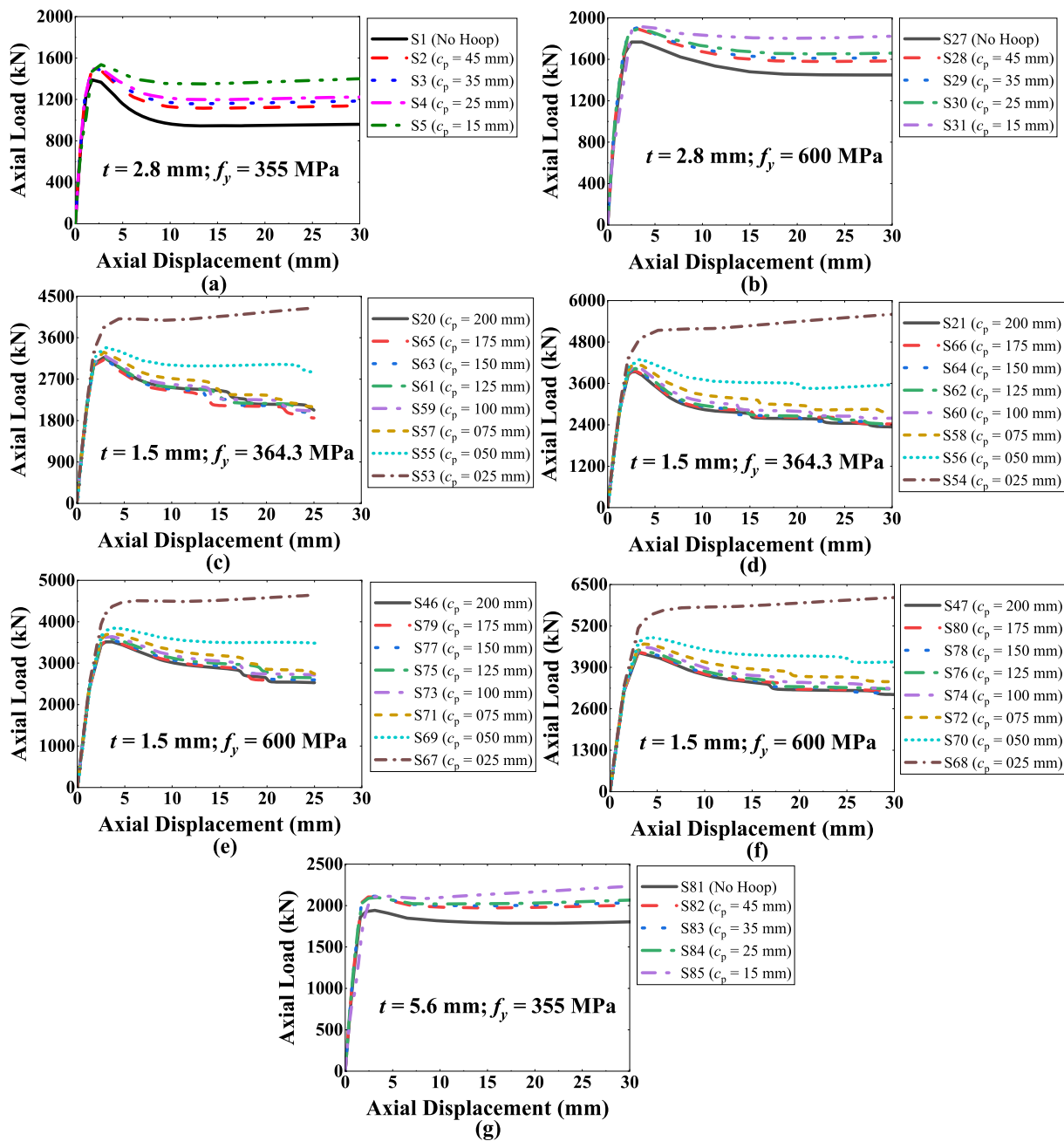

Fig. 13. Effect of transverse reinforcement spacing on compression behaviour for: (a) S1–S5, (b) S27–S31, (c) S20, S53, S55, S57, S59, S61, S63, and S65, (d) S21, S54, S56, S58, S60, S62, S64, and S66, (e) S46, S79, S77, S75, S73, S71, S69, and S67, (f) S47, S80, S78, S76, S74, S72, S70, and S68, and (g) S81, S82, S83, S84, and S85.
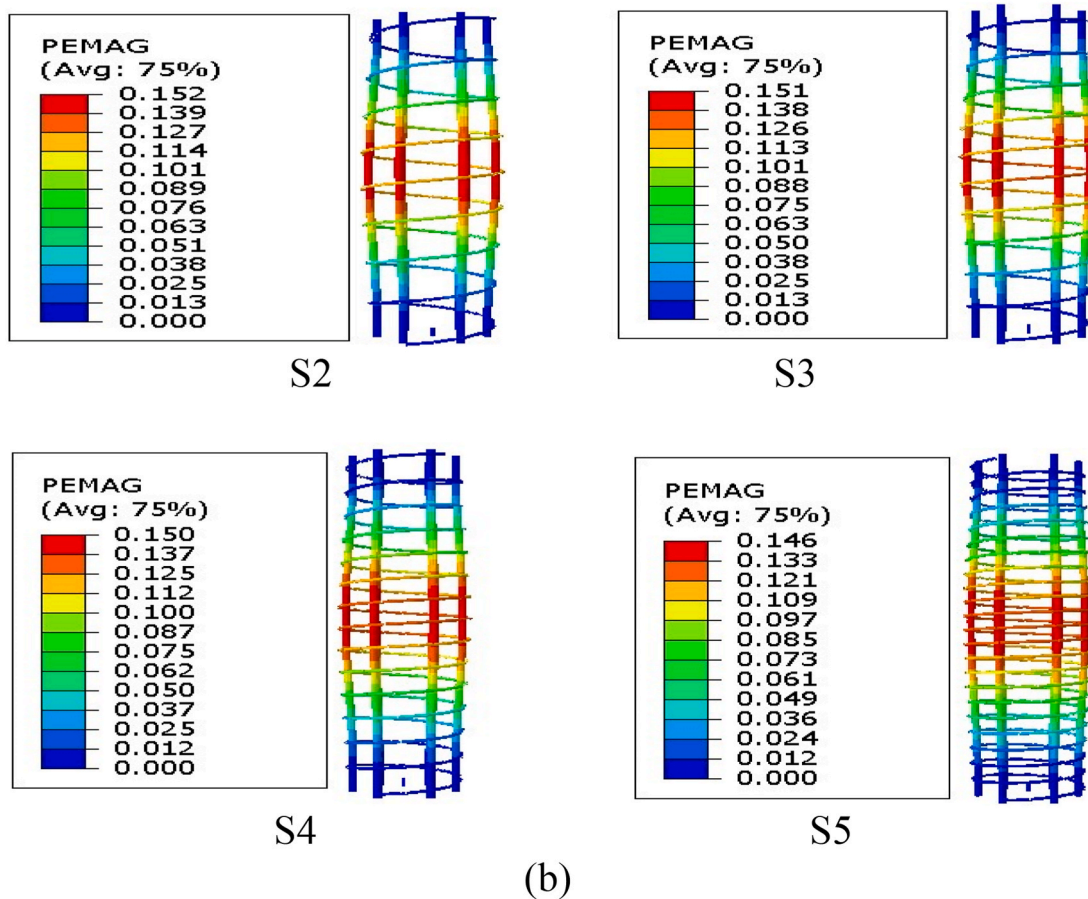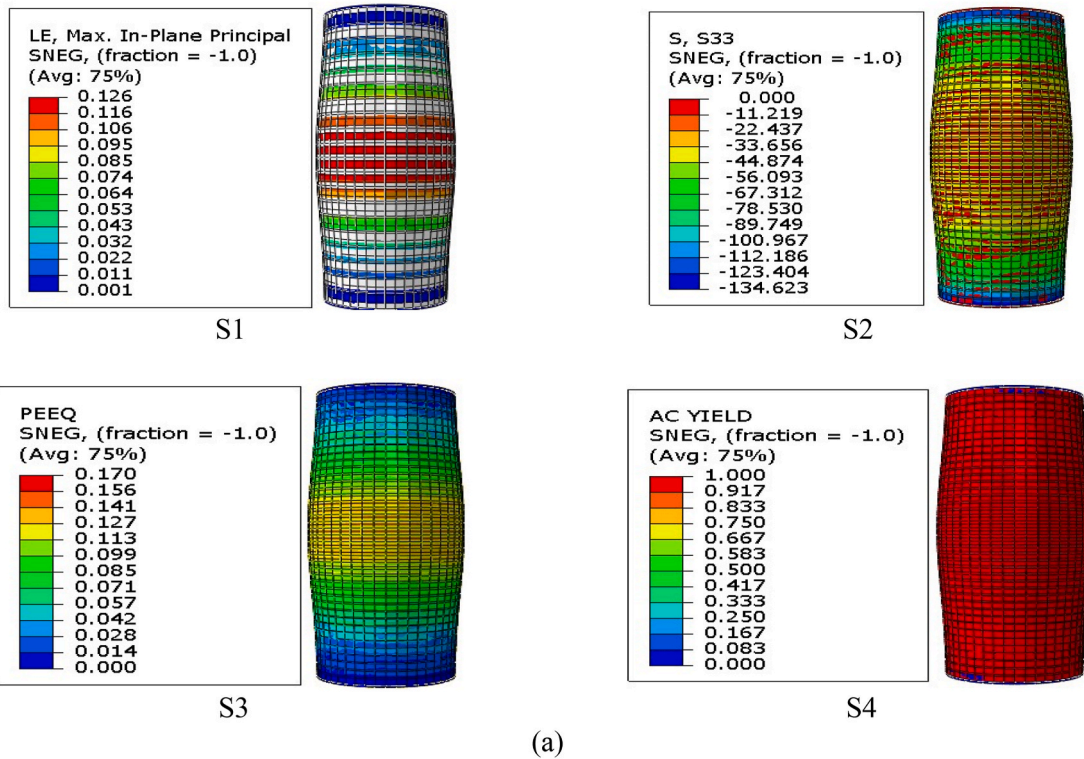
Fig. 14. Effect of amount of longitudinal reinforcements: (a) S1 (Mises stress distribution), S2 (longitudinal stress distribution), S3 (plastic strain equivalent distribution), and S4 (active yield), (b) plastic strain magnitude, and (c) axial stress.
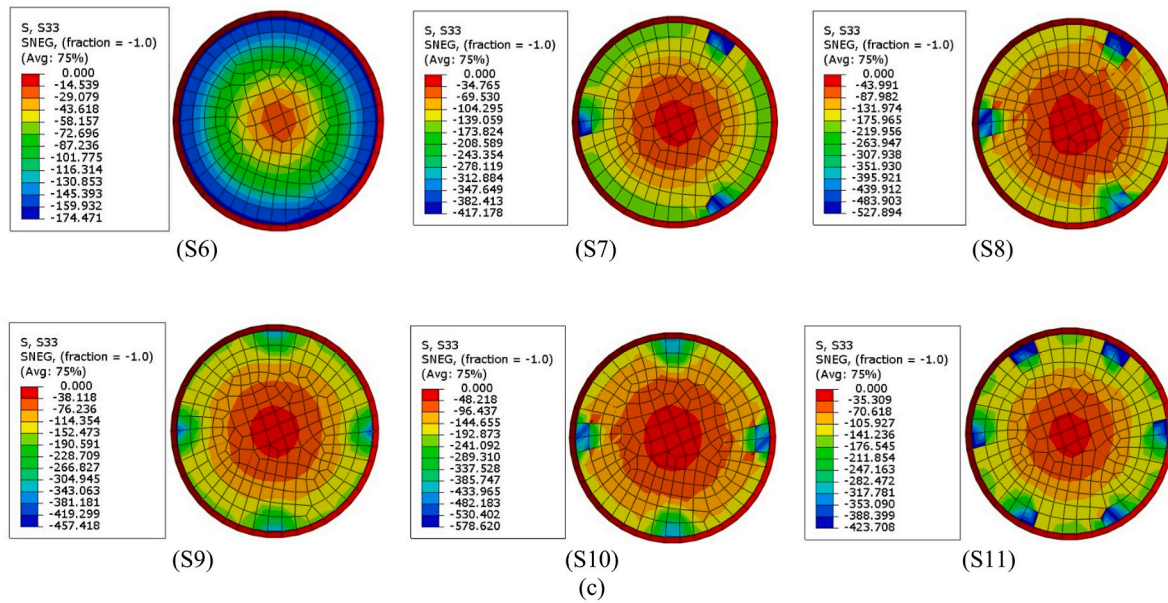
(S6)   (S7)   (S8)

(S9)   (S10)   (S11)

(c)

Fig. 14. (*continued*).

confinement provided by the steel tube, the column's failure mode is dependent on the degree of axial compression. However, the results of this study are consistent with most experimental studies where the stiffness and ductility of the section, as well as the load and energy dissipation capacities, increased with an increase in the steel tube yield strength [67,68].

It is important to state that the core concrete was normally crushed in the tension region, while the localised buckling of the steel tube mostly occurred in the mid-height section. As a result, an improvement in the ductility and compression capacity with increasing the steel tube yield strength could be explained. This is because the steel tube exhibited strong lateral compressive stress due to larger dilatation of the concrete with higher yield strength. Additionally, due to the positive impact of high strength steel tube on the ductility, the RCFST columns with larger steel yield strength behaved in a good ductile manner. Ultimately, the ultimate load capacity and ductility of the RCFST columns were improved with increasing the yield strength of the steel tube.

3.2. Effect of spacing of transverse reinforcement

Fig. 13 demonstrates the effect of the transverse reinforcement spacing on the behaviour of FEMs when subjected to axial compression. From Fig. 13(a), it can be seen that all the FEMs share a similar ascending portion, however, the descending portion of the FEMs is where there is the main difference. The use of a transverse reinforcement in the columns clearly has a substantial impact on the columns' post-yield behaviour. Furthermore, the post-yield behaviour of the columns is significantly impacted by spacing of the transverse reinforcement. Similar pattern is witnessed when the yield strength of the outer steel tube increased to 600 MPa (Fig. 13(b)) and when the thickness of the steel tube increased to 5.6 mm in Fig. 13(g).

Fig. 13(d) depicts that FEM S21, with a transverse reinforcement spacing of 200 mm, has a compression capacity of 3939.77 kN, while FEM S54, with a transverse reinforcement spacing of 25 mm, has a compression capacity of 5600.84 kN. At compression capacity level, S21 has axial displacement of 2.94 mm, while S54 behaved in a more ductile manner and has the axial displacement of 30 mm. The compression capacity and axial displacement attained for FEM S66, S64, S62, S60, S58, and S56 are 3962.72 kN and 2.9 mm, 3992.31 kN and 2.9 mm, 4033.03 kN and 2.9 mm, 4078.8 kN and 2.9 mm, 4164.87 kN and 2.9 mm, and 4306.96 kN and 3.42 mm, respectively. According to these

observations, it is demonstrated that the compression capacity increases as the transverse reinforcements' spacing reduces, whereas the axial displacement for S21, S66, S64, S62, S60, and S58 remains constant and increases for S56 and S54. Fig. 13(c), (e), and (f) show a similar pattern. Because the outer steel tube diameter for FEMs in Fig. 13(d) is larger than FEMs in Fig. 13(c), it performs better than FEMs in Fig. 13(c). Due to an increase in the yield strength of the steel tubes, FEMs in Fig. 13(e) and (f) perform better than FEMs in Fig. 13(c) and (d).

In line with the earlier research, the CFST columns with the widest transverse reinforcement spacing had smaller steel ratios, and the confining effect on the core concrete was insufficient. It had an impact on the increase in its bearing capacity [69]. The strain development of the longitudinal reinforcement was greater than that of the steel tube at the start of loading [69], while the strain development speed slowed down, the steel tube yielded, and the longitudinal strain increased before the peak point, delaying the excessive deformation of the steel tube and the quick decline in the specimens' bearing capacity. The transverse cage's reinforcing confinement impact on the core concrete became more apparent as the transverse reinforcement spacings became smaller (80 mm – 50 mm), which increased the specimens' bearing capacity and peak strain. Besides, performance in terms of the energy dissipation and ductility was also enhanced [69]. Similarly, lower lateral displacements for close range explosions or small-scale distances come from reduced transverse reinforcement spacing in RC columns under blast and axial loading [70]. Overall, it can be mentioned that the RCFST columns' compression capacity increased as the transverse reinforcement spacing decreased.

In Fig. 14(a), for example, S1 is FEM with no longitudinal and transverse reinforcements. It can be observed from S1 that the specimen yielded at Mises stress of 0.126 MPa from the central region to both ends under the ultimate axial compression compared to S2 and S3 in Fig. 14 (a), where the specimens did not yield at the ultimate axial compression based on Mises stress and plastic strain equivalent. The reasons are that the load was gradually increased, which caused the longitudinal stress in the steel tube to be generally distributed in a band. Eventually, the steel tube reached the proportional limit because the tension side of the steel tube was under less stress than the compression side. At this moment, the longitudinal stress was dispersed in a band, the specimen was crushed, and the concrete was equally stressed. The concrete columns and steel tubes caused the elastic-plastic and yield stages, respectively, at a load increase to 75% of the peak load. When the specimen reached

its peak load, the concrete's plastic strain started to concentrate in the central region, while the Mises and longitudinal stress concentrations started at the middle of the specimen (tension zone) and gradually moved to both ends of the columns (compression zone). In addition, because the maximum stress was zero, the longitudinal stress had no impact on the yielding of the specimens S2–S4 (Fig. 14(a)). In comparison, the specimens S2, S3, S4, and S5 in Fig. 14(b) were FEMs with the transverse reinforcement spacings of 45 mm, 35 mm, 25 mm, and 15 mm, respectively. It is evident from Fig. 14(b) that the plastic strain magnitude decreased with increasing spacing of the transverse reinforcements. There were 0.66%, 1.32%, and 3.95% reductions in the plastic strain magnitude as the longitudinal and transverse reinforcement spacings reduced by 22.22%, 44.44%, and 66.67%, respectively. These results revealed that the capacity of the RCFST columns to resist permanent distortion, when their yield strength was exceeded, declined with increasing the transverse reinforcement spacing, resulting in the columns' buckling or failure.

Fig. 14(c) shows the specimens S6 to S11 with different numbers of the longitudinal reinforcements. It can be noticed from Fig. 14(c) that lower spacing of the transverse reinforcements increased the confinement effect on the concrete core, which increased the friction between the surfaces after cracking. These results indicated that the longitudinal and transverse reinforcements were principally in charge of resisting the horizontal and vertical forces in the tension zone, allowing the concrete inside the steel tube to transfer the compressive force, thereby increasing the loading area and decreasing the stress in the compression region [71]. Therefore, there was more resistance to the axial compressive load because of the larger friction forces and consequently, specimens performed better in the post-yield behaviour.

3.3. Effect of amount of longitudinal steel bars

The impact of the longitudinal steel bar quantity on the FEMs' performance under axial compression is presented in Fig. 15. As seen in Fig. 15(a), FEM S6 has a compression capacity of 1079.35 kN without the longitudinal steel bars, while S11, which is reinforced with six 8 mm diameter bars, has a compression capacity of 1249.5 kN. Both S6 and S11 have an equal axial displacement of 2.6 mm at the compression capacity level. Similar to S6 and S11, FEMs S7 and S9 have gradually increasing compression capacities of 1166.16 kN and 1194.31 kN, respectively, while maintaining the same axial displacement of 2.6 mm. The compression capacities of FEMs were further enhanced when the diameter of the bar was raised to 12 mm (Fig. 15 (b)); for S8, S10, and S12, the compression capacities are 1239.68 kN, 1291.85 kN, and 1416.78 kN, respectively. The axial displacements for S8 and S10 reduced to 2.28 mm at the compression capacity level; however, they increased to 20 mm for S12. Fig. 15(c) and (d) display a similar pattern, but with increased compression capacity values due to the increase in the steel tube thickness to 5.63 mm. Similar results are seen when the outer tube's yield strength was raised to 600 MPa, but with a substantially larger increase in the compression capacity values (Fig. 13(e)–(h)). These results are in line with the earlier research, which demonstrated that increasing the number and diameter of the longitudinal bars improved the columns' ability to support axial compression [69,71].

3.4. Effect of thickness of steel tube

Fig. 16 illustrates the influence of the steel tube thickness on the performance of FEMs under axial compression. In Fig. 16, the thickness of the outer steel tube for FEMs S1–S5 is 2.8 mm and for S81–S85, it is 5.6 mm. Fig. 16 depicts that when the steel tube thickness increased, the compression capacity of the FEMs enhanced as well. The reason is that using the steel tubes with a lower diameter to thickness ratio improves the confinement effect of the RCFST columns, increasing their ultimate axial strength. This supports a relevant study that found the compression capacity of RCFST slender columns was significantly lowered when the

diameter to thickness ratio of steel tubes increased [72]. In addition, according to a comparison of the literature with the present findings, an experimental study and mechanism analysis of square steel tubular columns reinforced by rhombic stirrups under axial compression demonstrated an improvement in the bearing capacity, energy dissipation, and ductility performance [69]. However, the peak strain and initial stiffness decreased with the increase of the steel tube thickness due to a considerable discrepancy in the strain of the longitudinal reinforcements, affecting the specimens' initial stiffness to a certain magnitude [69]. Despite these positive results, the thickness of the steel tube would be experimentally assessed to prevent local buckling or early failure if it exceeded a predetermined value.

3.5. Hyper parametric configuration of ML models

A trial-and-error tuning strategy was engaged to determine hyper parameters, architectures, and functions of the models during the training phase. Based on these results, the model with the highest average prediction accuracy over the entire training set was chosen. Table 4 summarises the optimal values of the resulting hyper parameter for the GB, RF, and KNN models. Using the trial-and-error method, the GPR model was tweaked, and two significant parameters were found: a gaussian noise of 0.05 and a width of the radial basis function of 0.38. There were 7 input nodes, 1 output node, and 6 hidden layer nodes in the ANN model. With 15 hidden neurons and a radial basis activation function, the ELM model provided the highest possible output. The ENN model's two emotional parameters were employed to achieve the best outcomes, and their values were determined through a process of trial and error as follows: the confidence value was 0.61, whereas the anxiety parameter was 0.36.

3.6. Performance indicators

The findings of the models developed for determining the ultimate load are presented in this section. Table 5 provides the R^2 and RMSE performance parameter values for each of the seven models for both the training and testing stages.

It should be emphasised that the goodness of fit of the built-in models was expressed by each model's training subset performance. It is evident from Table 5 that all the models performed very well in training stage. The performance of the ELM and ENN models was slightly lower when compared to the other five models in both the training and testing stages. The KNN model, whose performance was second best in the training stage, failed to do well in the testing stage. With $R^2 = 0.99925$ and RMSE = 0.00708 in the training stage and $R^2 = 0.99863$ and RMSE = 0.00717 in the testing stage, the highest modelling prediction performance was achieved by the GB model. Fig. 17 indicates the scatter plots of the developed models (GB, RF, KNN, GPR, ANN, ELM, and ENN) in the training and testing stages.

As displayed in Fig. 18, the performance of the developed models for both the training and testing stages can be examined using the Taylor diagram [73]. All the proposed models, with the exceptions of ELM and ENN, had good training performance, as evidenced by their positions in the Taylor's diagram (Fig. 18(a)), which were all relatively close to the reference point. Fig. 18(b) illustrates that the position of GB is closest to the reference point, corroborating the statistical findings that demonstrated the best performance of the GB model [45,49].

In the case of the current dataset, it was revealed that ANN outperformed both the ELM and ENN models. While ELM and ENN are seen as improvements above the ANN model, the specific qualities and complexities of the dataset might have benefited the ANN model's performance. It is vital to note that the performance of different models can vary depending on the nature of the dataset and the specific problem being addressed. Therefore, in this particular circumstance, the ANN model provided greater performance compared to the ELM and ENN models for the supplied dataset. The results of weights and biases of the
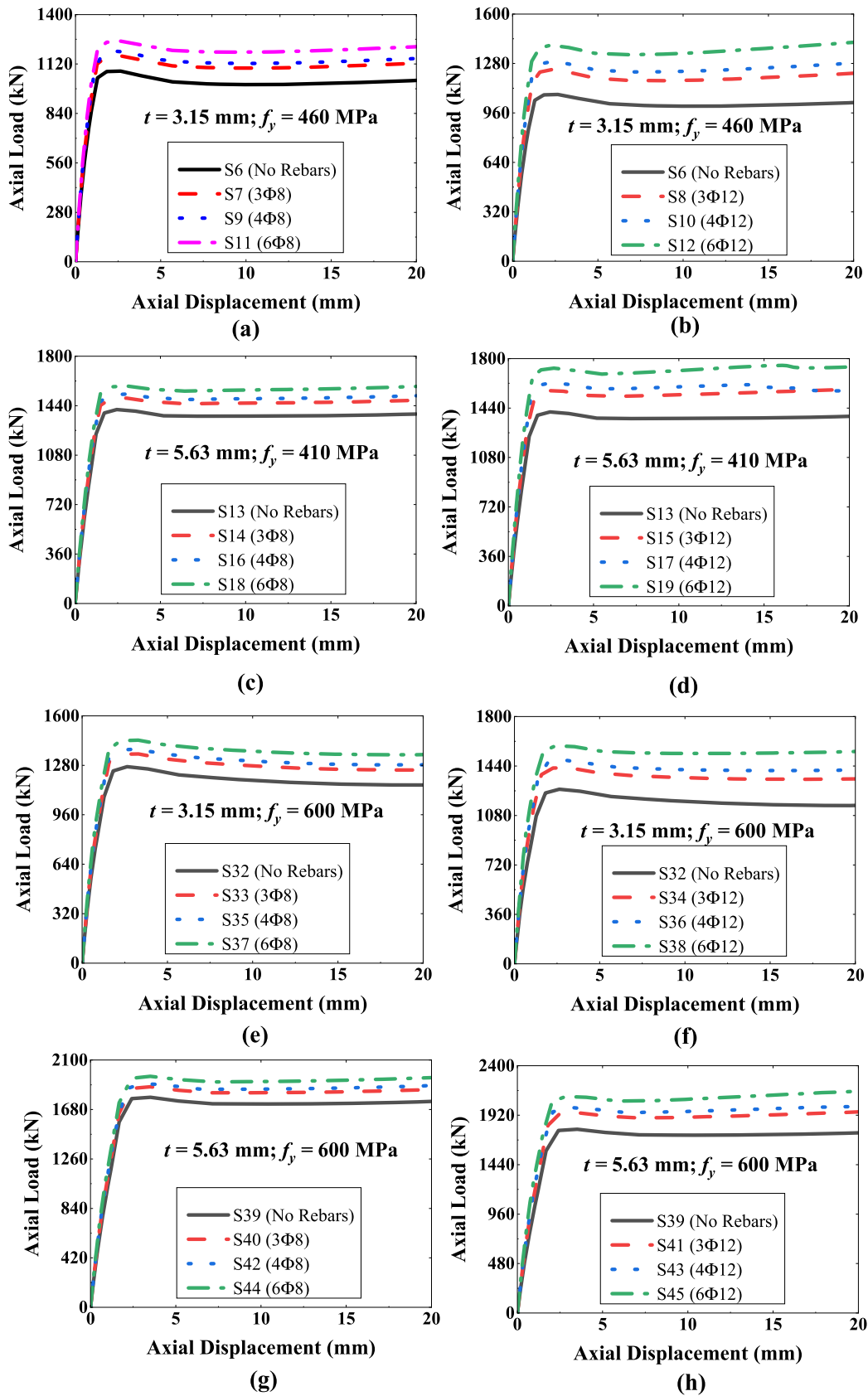
Fig. 15. Effect of amount of longitudinal steel bars on compression behaviour for: (a) S6, S7, S9, and S11, (b) S6, S8, S10, and S12, (c) S13, S14, S16, and S18, (d) S13, S15, S17, and S19, (e) S32, S33, S35, and S37, (f) S32, S34, S36, and S38, (g) S39, S40, S42, and S44, and (h) S39, S41, S43, and S45.
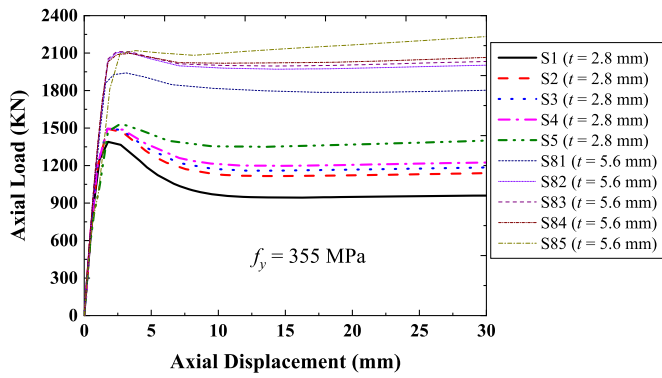
Fig. 16. Effect of steel tube thickness on compression behaviour.

Table 4
Hyper parameters of GB, RF, and KNN.

Model	Hyper parameter	Optimised value
GB	n_estimators	75
	max_features	3
	learning_rate	0.4
	min samples_leaf	5
	max depth	14
RF	n_estimators	80
	min_samples split	2
	max features	5
	max_depth	14
KNN	n _neighbours	3
	weights	distance
	leaf size	30
	p	1

Table 5
Performance of ML models in training and testing stages.

Model	Training		Testing	
	R^2	RMSE	R^2	RMSE
GB	0.99925	0.00708	0.99863	0.00717
RF	0.99657	0.01583	0.98656	0.02264
KNN	0.99905	0.00793	0.9754	0.03113
GPR	0.99893	0.00842	0.98968	0.01942
ANN	0.99708	0.01393	0.98068	0.02646
ELM	0.97665	0.0427	0.96678	0.04086
ENN	0.98943	0.02694	0.97367	0.03163

ANN model are presented in Equations 27–30:

$$w_1 = \begin{bmatrix} 1.08 & -0.46 & 1.34 & 1.04 & 0.30 & 0.25 & 0.98 \\ 0.88 & -0.19 & -0.09 & 0.58 & 0.34 & 0.49 & -0.37 \\ 0.07 & 1.03 & 0.70 & -0.19 & -0.04 & -0.68 & 1.30 \\ -0.40 & 0.61 & -0.30 & -0.26 & 0.92 & 0.70 & -0.87 \\ 0.67 & -1.30 & 1.20 & 0.98 & 0.22 & 0.94 & 0.83 \\ -0.69 & 1.02 & 1.39 & 0.71 & -0.47 & 0.10 & 1.16 \end{bmatrix} \quad (27)$$

$$w_2 = \begin{bmatrix} 0.12 & -0.02 & 0.20 & -0.21 & 0.36 & 0.57 \end{bmatrix} \quad (28)$$

$$b_1 = \begin{bmatrix} -1.39 \\ -0.45 \\ 0.64 \\ -0.75 \\ 0.64 \\ 1.26 \end{bmatrix} \quad (29)$$

$$b_2 = [0.49] \quad (30)$$

According to the ANN technique, the percentages of the relative relevance of the input parameters (inputs 1, 2, 3, 4, 5, and 7) are 6.79,

9.09, 39.26, 4.41, 8.21, and 21.24, respectively. The results from the RF model are 1.85, 5.89, 50.61, 2.20, 1.82, 1.78, and 35.83, respectively. Based on the relative relevance value derived using the ANN and RF models, inputs 3 and 7 are the most significant or have the greatest impact on the output. The network topology of ANN, depicted in Fig. 19, allows one to observe the relative importance of the input parameters. The considerable width of connections in black, which denotes their dominance in deciding the outputs, makes it clear that inputs 3 and 7 have a noticeable relative relevance, which is also indicated by their significance in influencing the outputs.

This finding is consistent with the observation from the Pearson correlation heat map (Fig. 11), which demonstrates that inputs 3 and 7 have the highest correlation with the output variable. The high correlation suggests a strong linear relationship between these inputs and the output. Therefore, any changes or variations in inputs 3 and 7 are likely to have a significant impact on the predicted output of the model. Furthermore, using the SHAP analysis process, the contribution of features to each prediction is explained using Shapley values, which are obtained through the application of the game theory coalitions [74]. Figs. 20 and 21 show the SHAP global explanations and mean absolute SHAP values of the KNN model, which indicate the dominance of inputs 3 and 7 in predicting the output.

4. Conclusions

The axial compressive behaviour- of the RCFST columns was examined in this research work. The used parameters were the steel tube's yield strength, transverse reinforcements' pitch spacing, number of the longitudinal bars, and thickness of the steel tube. Furthermore, seven ML models were created using data from FEMs and seven input features to predict the ultimate load. The following conclusions can be drawn:

i. Compression capacity of the RCFST columns increased with decreasing the transverse reinforcement spacing.
ii. The compressive strength and ductility of the RCFST columns were improved by increasing the yield strength and thickness of the steel tube as well as the number of the longitudinal reinforcing bars.
iii. Relationship between the FEMs and experimental results yielded a strong correlation with R^2 of 98.90%.
iv. All the ML models performed very well in the training stage. However, in both the training and testing stages, the ELM and ENN models' performance was marginally lower than that of the other five models. The GB model had the best modelling prediction performance in both the training and testing stages with R^2 of 0.99925 and 0.99863, respectively.
v. According to the relatively significant value calculated using the ANN and RF models, any variations in the concrete core areas and columns' height remarkably affected ultimate load.

The study demonstrated the effectiveness of the finite element analysis to model the relationship between the axial load and axial displacement. The FEMs suggested in this work could accurately depict the behaviour of the RCFST columns because findings from the literature supported the prediction accuracy of the finite element modelling. Using the ML techniques to predict the ultimate load of the RCFST columns can enable the columns' performance prediction with unknown properties by ML technique; this can augment the standard empirical models by providing the prediction findings, more quickly and easily. This method can help with timesaving, increased time efficiency, and theoretical and practical guidances for improving the RCFST columns' properties. Despite all these benefits, environmental conditions (temperature and humidity) and other materials' properties, which may influence the behaviour of the RCFST columns can be investigated in future research.
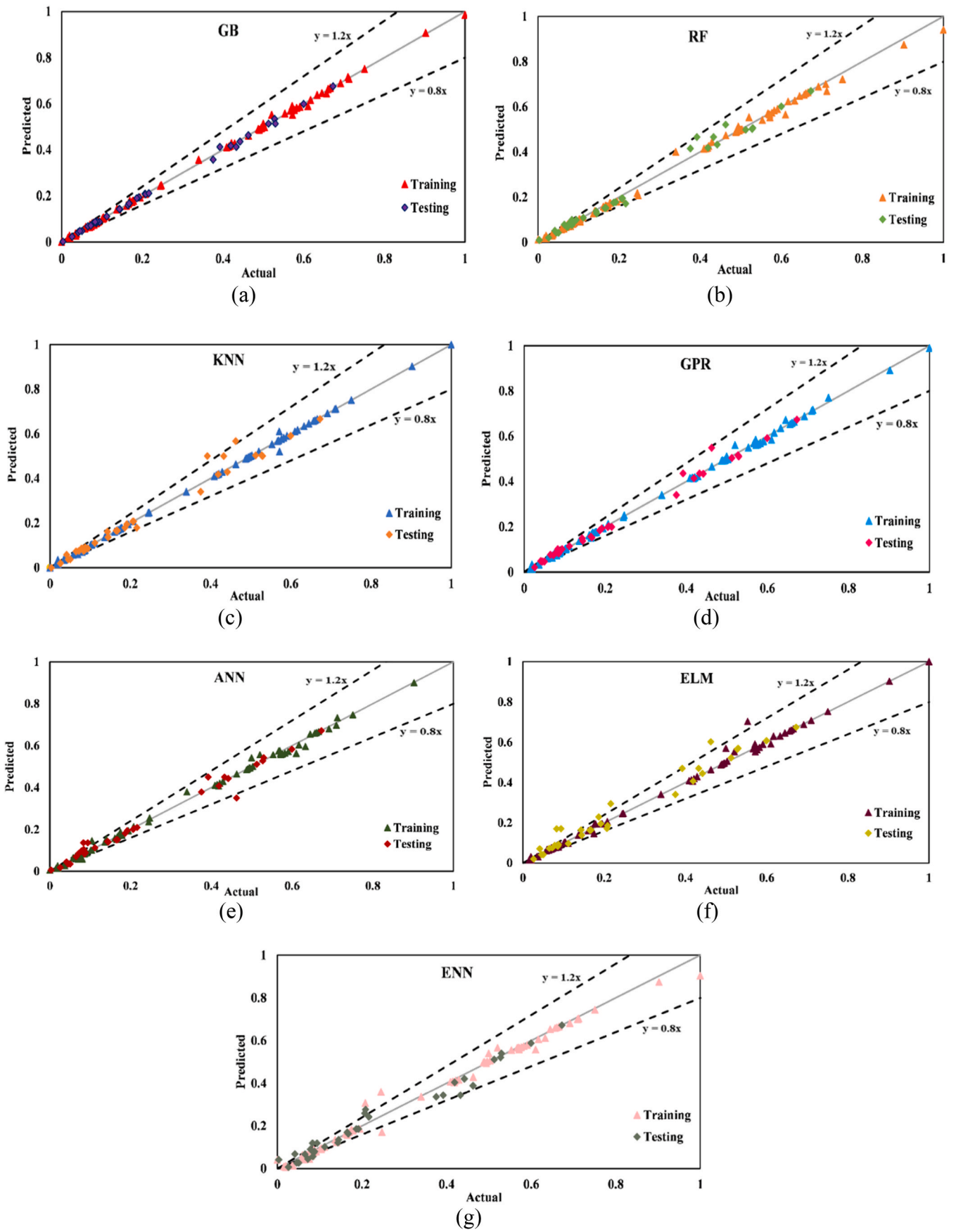
Fig. 17. Scatter plots for: (a) GB, (b) RF, (c) KNN, (d) GRP, (e) ANN, (f) ELM, and (g) ENN models.
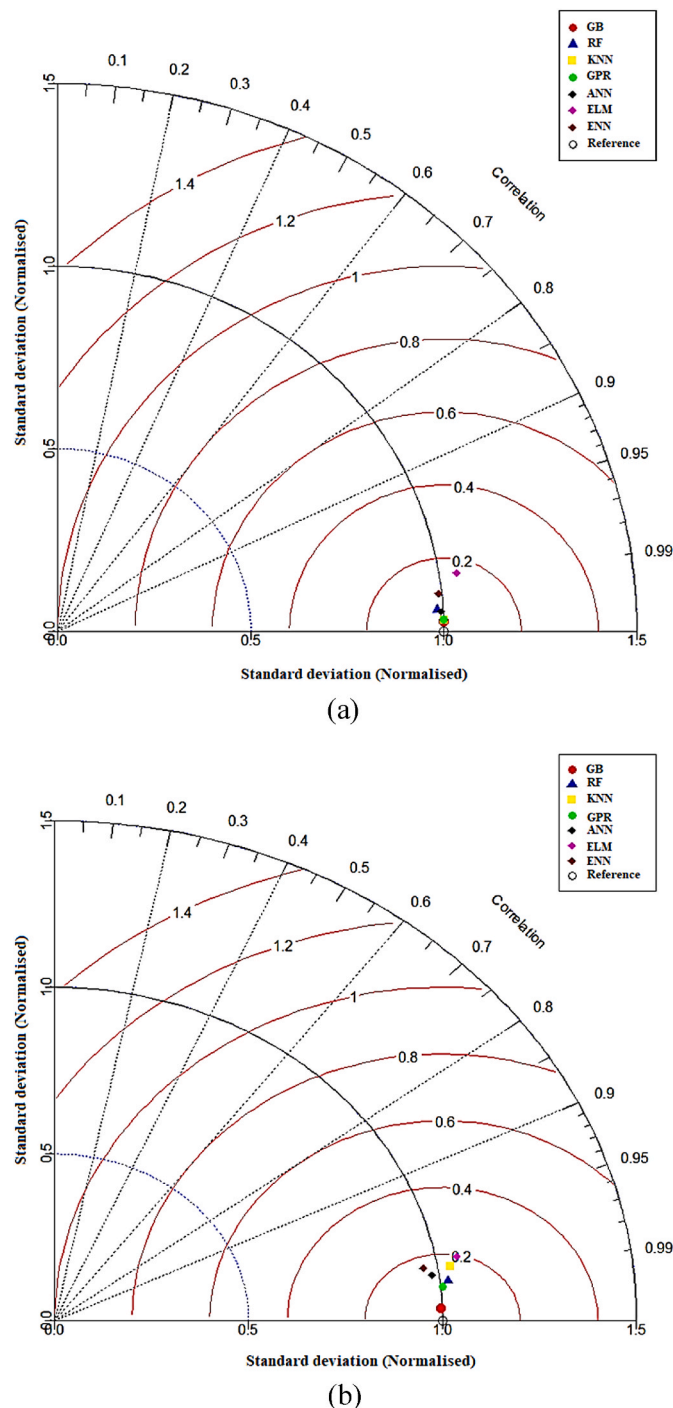
(a)

(b)

Fig. 18. Taylor diagram of developed models for: (a) training stage and (b) testing stage.

Author contributions

Conceptualization, H.I., A.B., and R.K.; data curation, H.I., N.C., A.B., and T.Q.; formal analysis, H.I., A.B., T.Q., and R.K.; funding, H.I. and A.B.; investigation, H.I., N.C., A.B., and T.Q.; methodology, H.I., N.C., A.B., and R.K.; project administration, H.I., N.C., A.B., T.Q., and R.K.; resources, H.I., N.C., A.B., T.Q., and R.K.; software, H.I., N.C., A.B., T.Q., and R.K.; supervision, H.I. and A.B.; validation, N.C., A.B., T.Q., and R.K.; visualization, N.C., A.B., S.O., T.Q., and R.K.; writing—original draft preparation, N.C., A.B., S.O., T.Q., and R.K.; writing—review and editing, N.C., A.B., S.O., T.Q., and R.K.; All authors have read and agreed to the published version of the manuscript.

Declaration of competing interest

The authors declare that they have no known competing financial interests or personal relationships that could affect the content of this research.
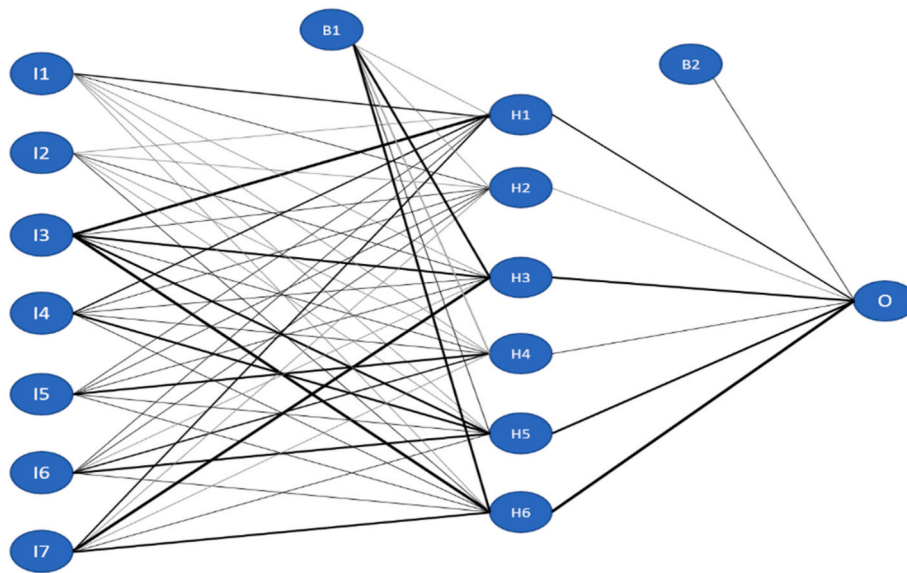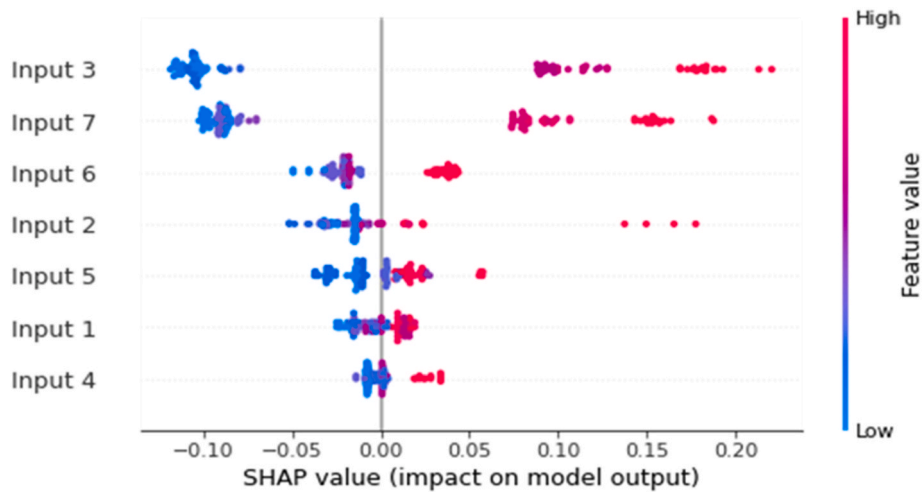
Fig. 19. Proposed architecture of ANN.

Fig. 20. SHAP global explanation of KNN model.

Data availability

Data will be made available on request.

Notations

A_c	Cross-sectional area of concrete
A_s	Cross-sectional area of steel tube
CDP	Concrete damaged plasticity
CFST	Concrete filled steel tube
c_p	Centre-centre spacing of transverse steel bar
D	Diameter of steel tube
d_b	Diameter of longitudinal steel bar
d_p	Diameter of transverse steel bar
e	Flow potential eccentricity
E_c	Modulus of elasticity of concrete
E_{sec}	Secant modulus of concrete
f_B	Confining stress
f_c'	Cylinder compressive strength of concrete
FEM	Finite element model
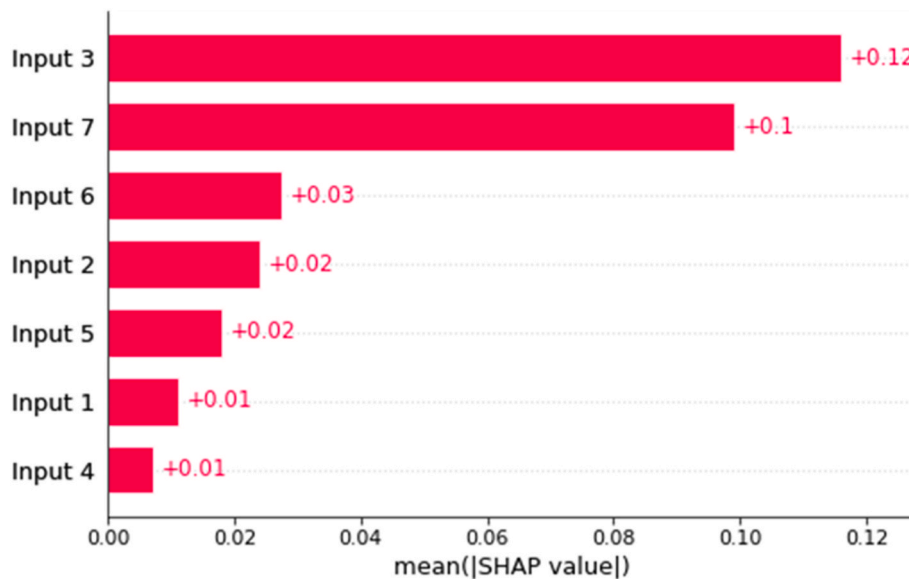
Fig. 21. Mean absolute SHAP values of KNN model.

f_t	Tensile strength of concrete
f_y	Yield strength of steel tube
f_{b0}/f_c'	Ratio of compressive strength under biaxial loading to uniaxial compressive strength
K_c	Ratio of second stress invariant on tensile meridian to compressive meridian
n	Number of longitudinal steel bar
RC	Reinforced concrete
RCFST	Reinforced concrete filled steel tube
t	Thickness of steel tube
s_p	Clear pitch spacing
β	Concrete stress block's effective height factor
k	Initial stiffness
ξ_s	Confinement factor
ε_{co}	Peak strain of unconfined concrete
ε_{cc}	Peak strain of confined concrete
ε_{ct}	Tensile strain of unconfined concrete corresponding to f_t
α	Ratio for reducing strength of concrete stress block
α_t	Concrete area to steel tube ratio
ψ	Dilation angle
ε	Strain
σ	Stress

References

[1] T. Tufan, H. Köten, Accelerometer mass loading study based on a damage identification method using fundamental laws in closed systems, J. Polytechnic 26 (2) (2023) 569–582.
[2] T. Tufan, H. Köten, An analysis on mode excitation energy in beam-like structures, J. Energy Syst. 6 (1) (2022) 84–96.
[3] J. Liu, X. Zhou, Behavior and strength of tubed RC stub columns under axial compression, J. Constr. Steel Res. 66 (2010) 28–36, https://doi.org/10.1016/j.jcsr.2009.08.006.
[4] S. Zhang, J. Liu, Seismic behavior and strength of square tube confined reinforced concrete (STRC) columns, J. Constr. Steel Res. 63 (2007) 1194–1207, https://doi.org/10.1016/j.jcsr.2006.11.017.
[5] A.M. Erfan, R.M. Abd Elnaby, A. Elhawary, T.A. El-Sayed, Improving the compressive behavior of RC walls reinforced with ferrocement composites under centric and eccentric loading, Case Stud. Constr. Mater. 14 (2021), e00541, https://doi.org/10.1016/j.cscm.2021.e00541.
[6] T.A. El-Sayed, Axial compression behavior of ferrocement geopolymer HSC columns, Polymers 13 (21) (2021) 3789, https://doi.org/10.3390/polym13213789.
[7] S.M. Davoodnabi, S.M. Mirhosseini, M. Shariati, Analyzing shear strength of steel-concrete composite beam with angle connectors at elevated temperature using finite element method, Steel Compos. Struct. 40 (6) (2021) 853–868, https://doi.org/10.12989/scs.2021.40.6.853.

[8] M.R. Hamidian, M.Z. Jumaat, U.J. Alengaram, N.H. Ramli Sulong, P. Shafigh, Pitch spacing effect on the axial compressive behaviour of spirally reinforced concrete-filled steel tube (SRCFT), Thin-Walled Struct. 100 (2016) 213–223, https://doi.org/10.1016/j.tws.2015.12.011.
[9] GB 50011-2001, GB 50011-2001 Code for Seismic Design of Buildings, GB50011 ed., Ministry of Construction China, 2001.
[10] E. Hosseinpour, S. Baharom, W.H.W. Badaruzzaman, M. Shariati, A. Jalali, Direct shear behavior of concrete filled hollow steel tube shear connector for slim-floor steel beams, Steel Compos. Struct. 26 (4) (2018) 485–499, https://doi.org/10.12989/scs.2018.26.4.485.
[11] W. Hua, H.J. Wang, A. Hasegawa, Y. Shioi, S. Iwasaki, Y. Miyamoto, Study on strength of reinforced concrete filled circular steel tubular columns, Struct. Eng. Mech. 19 (2005) 653–677, https://doi.org/10.12989/SEM.2005.19.6.653.
[12] A. Xiamuxi, A. Hasegawa, A. Xiamuxi, A. Hasegawa, Compression test of RCFT columns with thin-walled steel tube and high strength concrete, Steel Compos. Struct. 11 (2011) 391, https://doi.org/10.12989/SCS.2011.11.5.391.
[13] A. Xiamuxi, A. Hasegawa, A study on axial compressive behaviors of reinforced concrete filled tubular steel columns, J. Constr. Steel Res. 76 (2012) 144–154, https://doi.org/10.1016/J.JCSR.2012.03.023.
[14] M. Tomii, K. Sakino, Y. Xiao, Ultimate moment of reinforced concrete short columns confined in steel tube, in: Proceedings of the Pacific Conference on Earthquake Engineering, 1987.
[15] K. Sakino, Y. Sun, A. Aklan, Effects of wall thickness of steel tube on the behavior of square tubed R/C columns, in: Proceedings of the 11th World Conference on Earthquake Engineering, 1996.

[16] R.S. Aboutaha, R.I. Machado, Seismic resistance of steel-tubed high-strength reinforced concrete columns, J. Struct. Eng. 125 (1999) 485–494, https://doi.org/10.1061/(ASCE)0733-9445, 1999)125:5(485.

[17] S. Zhang, Seismic behavior and strength of square tube confined reinforced concrete (STRC) columns, J. Constr. Steel Res. 63 (2007) 1194–1207, https://doi.org/10.1016/J.JCSR.2006.11.017.

[18] X. Zhou, S. Zhang, J. Liu, Seismic behavior and steel tube confined reinforced-concrete beam–columns, J. Build. Struct. 29 (2008) 19–28.

[19] J. Liu, X. Zhou, Behavior and strength of tubed RC stub columns under axial compression, J. Constr. Steel Res. 66 (2010) 28–36, https://doi.org/10.1016/J.JCSR.2009.08.006.

[20] X. Wang, J. Liu, S. Zhang, Behavior of short circular tubed-reinforced-concrete columns subjected to eccentric compression, Eng. Struct. 105 (2015) 77–86, https://doi.org/10.1016/J.ENGSTRUCT.2015.10.001.

[21] M.R. Hamidian, M.Z. Jumaat, U.J. Alengaram, N.H. Ramli Sulong, P. Shafigh, Pitch spacing effect on the axial compressive behaviour of spirally reinforced concrete-filled steel tube (SRCFT), Thin-Walled Struct. 100 (2016) 213–223, https://doi.org/10.1016/J.TWS.2015.12.011.

[22] H.G. Hasan, T. Ekmekyapar, B.A. Shehab, Mechanical performances of stiffened and reinforced concrete-filled steel tubes under axial compression, Mar. Struct. 65 (2019) 417–432, https://doi.org/10.1016/J.MARSTRUC.2018.12.008.

[23] Z. Tao, Z.-B. Wang, Q. Yu, Finite element modelling of concrete-filled steel stub columns under axial compression, J. Constr. Steel Res. 89 (2013) 121–131, https://doi.org/10.1016/j.jcsr.2013.07.001.

[24] L.-H. Han, G.-H. Yao, Z. Tao, Performance of concrete-filled thin-walled steel tubes under pure Torsion, Thin-Walled Struct. 45 (2007) 24–36, https://doi.org/10.1016/j.tws.2007.01.008.

[25] Q. Ren, M. Li, M. Zhang, Y. Shen, W. Si, Prediction of ultimate axial capacity of square concrete-filled steel tubular short columns using a hybrid intelligent algorithm, Appl. Sci. 9 (2019) 2802, https://doi.org/10.3390/app9142802.

[26] P. Sarir, J. Chen, P.G. Asteris, D.J. Armaghani, M.M. Tahir, Developing GEP tree-based, neuro-swarm, and whale optimization models for evaluation of bearing capacity of concrete-filled steel tube columns, Eng. Comput. 37 (2021) 1–19, https://doi.org/10.1007/s00366-019-00808-y.

[27] L. Ma, C. Zhou, D. Lee, J. Zhang, Prediction of axial compressive capacity of CFRP-confined concrete-filled steel tubular short columns based on XGBoost algorithm, Eng. Struct. 260 (2022), 114239, https://doi.org/10.1016/j.engstruct.2022.114239.

[28] D.B. Zewdu, A.T. Wondimu, Numerical investigation of carbon fiber reinforced polymer confined concrete-filled steel tube columns under eccentric load, Adv. Civ. Eng. (2022) 1–15, https://doi.org/10.1155/2022/4807436, 2022.

[29] X. Zhou, J. Liu, X. Wang, Y.F. Chen, Behavior and design of slender circular tubed-reinforced-concrete columns subjected to eccentric compression, Eng. Struct. 124 (2016) 17–28, https://doi.org/10.1016/j.engstruct.2016.05.036.

[30] W. Ramberg, W.R. Osgood, Description of Stress-Strain Curves by Three Parameters, 1943.

[31] H.F. Isleem, P. Jagadesh, J. Ahmad, S. Qaidi, F. Althoey, H.M. Najm, M.M.S. Sabri, Finite element and analytical modelling of PVC-confined concrete columns under axial compression, Front. Mater. 9 (2022), 1011675, https://doi.org/10.3389/fmats.2022.1011675.

[32] ABAQUS SIMULIA User Assistance 2017, Dassault Systems Similia Corp; Johnston, Ed.; ABAQUS: United States.

[33] H.F. Isleem, P. Jagadesh, S. Qaidi, F. Althoey, C. Rahmawati, H.M. Najm, M.M.S. Sabri, Finite element and theoretical investigations on PVC-CFRP confined concrete columns under axial compression, Front. Mater. 9 (2022), https://doi.org/10.3389/fmats.2022.1055397.

[34] N.D.K.R. Chukka, B.S. Reddy, K. Vasugi, Y.B.S. Reddy, L. Natrayan, S. Thanappan, Experimental testing on mechanical, durability and adsorption dispersion properties of concrete with multiwalled carbon nanotubes and silica fumes, Adsorpt. Sci. Technol. (2022) 4347753, https://doi.org/10.1155/2022/4347753.

[35] H.F. Isleem, B.O. Yusuf, W. Xingchong, T. Qiong, P. Jagadesh, D.S. Augustino, Analytical and numerical investigation of polyvinyl chloride (PVC) confined concrete columns under different loading conditions, Aust. J. Struct. Eng. (2023) 1–29, https://doi.org/10.1080/13287982.2023.2216566.

[36] H.F. Isleem, M. Abid, W.S. Alaloul, M.K. Shah, S. Zeb, M.A. Musarat, M.F. Javed, F. Aslam, H. Alabduljabbar, Axial compressive strength models of eccentrically-loaded rectangular reinforced concrete columns confined with FRP, Materials 14 (2021) 3498, https://doi.org/10.3390/ma14133498.

[37] Q. Han, W. Wang, Z. Guo, Y. Wu, J. Chen, Experimental study on the axial compressive behavior of elliptical double skin steel tube concrete columns, J. Constructional Steel Res. 183 (2021), 106481.

[38] ACI 318-11 Building Code Requirements for Structural Concrete (ACI 318-11) and Commentary; MI, Farmington Hills, USA, 2011.

[39] V.K. Papanikolaou, A.J. Kappos, Confinement-sensitive plasticity constitutive model for concrete in triaxial compression, Int. J. Solid Struct. 44 (2007) 7021–7048, https://doi.org/10.1016/J.IJSOLSTR.2007.03.022.

[40] A.K. Samani, M.M.A. Attard, Stress–strain model for uniaxial and confined concrete under compression, Eng. Struct. 41 (2012) 335–349, https://doi.org/10.1016/J.ENGSTRUCT.2012.03.027.

[41] B. De Nicolo, L. Pani, E. Pozzo, Strain of concrete at peak compressive stress for a wide range of compressive strengths, Mater. Struct. 27 (1994) 206–210.

[42] B. Binici, An analytical model for stress–strain behavior of confined concrete, Eng. Struct. 27 (2005) 1040–1051, https://doi.org/10.1016/J.ENGSTRUCT.2005.03.002.

[43] F. Aslani, R. Jowkarmeimandi, Stress–strain model for concrete under cyclic loading, Mag. Concr. Res. 64 (2012) 673–685, https://doi.org/10.1680/MACR.11.00120.

[44] L. Breiman, J.H. Friedman, R.A. Olshen, C.J. Stone, Classification and Regression Trees. Classification and Regression Trees, LEO-BREIMAN, 2017, https://doi.org/10.1201/9781315139470/CLASSIFICATION-REGRESSION-TREES-, 1–358.

[45] R. Kumar, B. Rai, P.A. Samui, Comparative study of prediction of compressive strength of ultra-high performance concrete using soft computing technique, Struct. Concr. (2023), https://doi.org/10.1002/SUCO.202200850.

[46] L. Auret, C. Aldrich, Interpretation of nonlinear relationships between process variables by use of random forests, Miner. Eng. 35 (2012) 27–42, https://doi.org/10.1016/J.MINENG.2012.05.008.

[47] J. Zhang, G. Ma, Y. Huang, J. sun, F. Aslani, B. Nener, Modelling uniaxial compressive strength of lightweight self-compacting concrete using random forest regression, Construct. Build. Mater. 210 (2019) 713–719, https://doi.org/10.1016/J.CONBUILDMAT.2019.03.189.

[48] J.H. Friedman, Greedy function approximation: a gradient boosting machine, AOS (Acta Odontol. Scand.) (2001) 1189–1232, https://doi.org/10.1214/AOS/1013203451.

[49] C. Bentejac, A. Csorgo, G. Martinez-Munoz, A comparative analysis of XGBoost, Artif. Intell. Rev. 54 (2019) 1937–1967, https://doi.org/10.1007/s10462-020-09896-5.

[50] C. Bentéjac, A. Csörgő, G. Martínez-Muñoz, A comparative analysis of gradient boosting algorithms, Artif. Intell. Rev. 54 (2021) 1937–1967, https://doi.org/10.1007/S10462-020-09896-5.

[51] Z.Y. Wan, T.P. Sapsis, Reduced-space Gaussian process regression for data-driven probabilistic forecast of chaotic dynamical systems, Physica D 345 (2017) 40–55, https://doi.org/10.1016/J.PHYSD.2016.12.005.

[52] N.D. Hoang, A.D. Pham, Q.L. Nguyen, Q.N. Pham, Estimating compressive strength of high performance concrete with Gaussian process regression model, Adv. Civ. Eng. (2016), https://doi.org/10.1155/2016/2861380, 2016.

[53] B.A. Omran, Q. Chen, R. Jin, Comparison of data mining techniques for predicting compressive strength of environmentally friendly concrete, J. Comput. Civ. Eng. 30 (2016), 04016029, https://doi.org/10.1061/(ASCE)CP.1943-5487.0000596.

[54] P.G. Asteris, A.D. Skentou, A. Bardhan, P. Samui, P.B. Lourenço, Soft computing techniques for the prediction of concrete compressive strength using non-destructive tests, Construct. Build. Mater. 303 (2021), 124450, https://doi.org/10.1016/J.CONBUILDMAT.2021.124450.

[55] K.W. Chau, C.L. Wu, Y.S. Li, Comparison of several flood forecasting models in yangtze river, J. Hydrol. Eng. 10 (2005) 485–491, https://doi.org/10.1061/(ASCE)1084-0699, 2005)10:6(485.

[56] H.F. Isleem, Feng Peng, B.A. Tayeh, W.S. Alaloul, M.A. Musarat, A. Raza, Artificial neural network (ANN) and finite element (FE) models for GFRP-reinforced concrete columns under axial compression, Materials 14 (2021) 7172, https://doi.org/10.3390/ma14237172.

[57] H.F. Isleem, B.A. Tayeh, M. Abid, M. Iqbal, A.M. Mohamed, M.G.E. Sherbiny, Finite element and artificial neural network modeling of FRP-RC columns under axial compression loading, Front. Mater. 9 (2022) 288, https://doi.org/10.3389/fmats.2022.888909.

[58] H.F. Isleem, D.S. Augustino, A.S. Mohammed, A.M. Najemalden, P. Jagadesh, S. Qaidi, M.M.S. Sabri, Finite element, analytical, artificial neural network models for carbon fibre reinforced polymer confined concrete filled steel columns with elliptical cross sections, Front. Mater. 9 (2023), https://doi.org/10.3389/fmats.2022.1115394.

[59] A. Bardhan, R. Biswas, N. Kardani, M. Iqbal, P. Samui, M.P. Singh, P.G. Asteris, A novel integrated approach of augmented grey wolf optimizer and ANN for estimating axial load carrying capacity of concrete-filled steel tube columns, Construct. Build. Mater. 337 (2022), 127454, https://doi.org/10.1016/J.CONBUILDMAT.2022.127454.

[60] S.K. Das, P. Samui, A.K. Sabat, Application of artificial intelligence to maximum dry density and unconfined compressive strength of cement stabilized soil, Geotech. Geol. Eng. 29 (2011) 329–342, https://doi.org/10.1007/S10706-010-9379-4/METRICS.

[61] S.K. Das, P. Samui, A.K. Sabat, Prediction of field hydraulic conductivity of clay liners using an artificial neural network and support vector machine, Int. J. GeoMech. 12 (2012) 606–611, https://doi.org/10.1061/(ASCE)GM.1943-5622.0000129.

[62] G.B. Huang, Q.Y. Zhu, C.K. Siew, Extreme learning machine: theory and applications, Neurocomputing 70 (2006) 489–501, https://doi.org/10.1016/J.NEUCOM.2005.12.126.

[63] A. Bardhan, N. Kardani, A.K. Alzo'ubi, B. Roy, P. Samui, A.H. Gandomi, Novel integration of extreme learning machine and improved harris hawks optimization with particle swarm optimization-based mutation for predicting soil consolidation parameter, JRMGE 14 (2022) 1588–1608, https://doi.org/10.1016/J.JRMGE.2021.12.018.

[64] A. Gholami, H. Bonakdari, P. Samui, M. Mohammadian, B. Gharabaghi, Predicting stable alluvial channel profiles using emotional artificial neural networks, Appl. Soft Comput. 78 (2019) 420–437, https://doi.org/10.1016/J.ASOC.2019.03.003.

[65] V. Nourani, An emotional ANN (EANN) approach to modeling rainfall-runoff process, J. Hydrol. (Amst.) 544 (2017) 267–277, https://doi.org/10.1016/J.JHYDROL.2016.11.033.

[66] E. Sharghi, V. Nourani, H. Najafi, A. Molajou, Emotional ANN (EANN) and wavelet-ANN (WANN) approaches for markovian and seasonal based modeling of rainfall-runoff process, Water Resour. Manag. 32 (2018) 3441–3456, https://doi.org/10.1007/S11269-018-2000-Y/METRICS.

[67] L. Jiang, W. Wang, J. Ji, H. Ren, Q. Wang, R. Sun, C. Yu, H. Zhang, G. Luo, Bearing behavior of high-performance concrete-filled high-strength steel tube composite columns subjected to eccentrical load, Front. Mater. 9 (2022), https://doi.org/10.3389/fmats.2022.972811.

[68] T. Zhang, Prediction and analysis of the residual capacity of concrete-filled steel tube stub columns under axial compression subjected to combined freeze–Thaw cycles and acid rain corrosion, Materials 12 (2019) 3070, https://doi.org/10.3390/ma12193070.

[69] Z. Chen, F. Ning, L. Mo, Experimental study and mechanism analysis of concrete-filled square steel tubular columns reinforced by rhombic stirrups under axial compression, Front. Mater. 8 (2021) 1–15, https://doi.org/10.3389/fmats.2021.646656.

[70] C. Kyei, A. Braimah, Effects of transverse reinforcement spacing on the response of reinforced concrete columns subjected to blast loading, Eng. Struct. 142 (2017) 148–168, https://doi.org/10.1016/j.engstruct.2017.03.044.

[71] Y. Lin, Z. Zhao, X. Gao, Z. Wang, S. Qu, Behavior of concrete-filled U-shaped steel beam to CFSST column connections, Buildings 13 (2023) 517, https://doi.org/10.3390/buildings13020517.

[72] J. Wang, F. Wang, Q. Shen, Numerical modelling and design recommendation of axially-loaded thin-walled RCFST slender column, Thin-Walled Struct. 135 (2019) 210–226, https://doi.org/10.1016/j.tws.2018.11.004.

[73] K.E. Taylor, Summarizing multiple aspects of model performance in a single diagram, J. Geophys. Res. Atmos. 106 (2001) 7183–7192, https://doi.org/10.1029/2000JD900719.

[74] L. Cavaleri, M.S. Barkhordari, C.C. Repapis, D.J. Armaghani, D.V. Ulrikh, P. G. Asteris, Convolution-based ensemble learning algorithms to estimate the bond strength of the corroded reinforced concrete, Construct. Build. Mater. 359 (2022), 129504, https://doi.org/10.1016/J.CONBUILDMAT.2022.129504.

[75] R. Kumar, B. Rai, P. Samui, Machine learning techniques for prediction of failure loads and fracture characteristics of high and ultra-high strength concrete beams, Innovat. Infrastruct. Solut. (2023) 8.